

General information of the article

Type of paper: Article

Title: Cyclic lateral response and failure mechanisms of a semi-rigid pile in soft clay: centrifuge tests and numerical modelling

Authors: Y. Hong¹, B. He², L.Z. Wang^{3*}, Z. Wang⁴, C.W.W. Ng⁵, D. Mašín⁶

*Corresponding author

Information of the authors

Corresponding author: Dr L.Z. Wang

Chair Professor, Key Laboratory of Offshore Geotechnics and Material of Zhejiang Province, College of Civil Engineering and Architecture, Zhejiang University, China

Email: wanglz@zju.edu.cn

Tel: (86) 13656676923

Co-author: Dr Y. Hong

Lecturer, Key Laboratory of Offshore Geotechnics and Material of Zhejiang Province, College of Civil Engineering and Architecture, Zhejiang University, China

Email: yi_hong@zju.edu.cn

Co-author: Dr B. He

Engineer, Power China Huadong Engineering Limited Corporation, China

Email: hebenzheda@126.com

Co-author: Dr Z. Wang

Engineer, Four harbor engineering institute Co. Ltd, China Communications

Construction Company, China

Email: wangzhanzju@163.com

Co-author: Dr C. W. W. Ng

Chair Professor, Department of Civil and Environmental Engineering, Hong Kong University of Science and Technology, HKSAR

Email: cecwwng@ust.hk

Co-author: Dr D. Mašín

Professor, Faculty of Science, Charles University in Prague, Czech Republic

Email: david.masin@natur.cuni.cz

Abstract

Previous studies on laterally loaded piles in clay have mainly focused on flexible and rigid piles. Little attention has been paid to semi-rigid piles (whose pile-soil stiffness lies somewhere between those of rigid and flexible piles), which may behave as either flexible piles or rigid piles, depending on the change in soil stiffness during cycling. This study aims to understand the cyclic lateral response of a repeatedly loaded semi-rigid pile in soft clay and the failure mechanisms of the soil around the pile, through a series of centrifuge model tests and 3D finite element analyses using an advanced hypoplastic clay model. Numerical parametric studies were also performed to investigate the evolution of soil flow mechanisms with increasing pile rigidity. It is revealed that the semi-rigid pile behaved as if it were a flexible pile (i.e., flexural deformation dominated) during the first few cycles, but tended to behave like a rigid pile (i.e., rotational movement prevailed) during subsequent cycles, which progressively softened the surrounding soil. As a result, the mechanisms of soil flow around the semi-rigid pile exhibited an intermediate behaviour combining the mechanisms of both flexible and rigid piles. Three distinctive mechanisms were identified: a wedge-type mechanism near the surface, a full-flow mechanism (within the transverse sections) near the middle of the pile, and a rotational soil flow mechanism (in the vertical symmetrical plane of the pile) near the lower half of the pile. By ignoring the rotational soil flow mechanism, which has a much lower resistance than the full-flow mechanism, the API (2007) code underestimated the cyclic bending moment and the lateral pile displacement by 10 and 69%, respectively. Application of jet-grouting around the semi-rigid pile at shallow depth significantly altered the soil flow mechanism (i.e., it was a solely wedge-type mechanism around the grouted zone).

Key words: centrifuge modelling, semi-rigid pile, cyclic loading, clays, failure modes

Introduction

A wide range of onshore and offshore infrastructures (such as transmission towers, onshore/offshore wind turbines, bridge piers and floating offshore platforms) face repeated loading by horizontal forces from the wind, waves and currents. The wide range of loading magnitudes imposed on these infrastructures has led to the design of pile foundations with various levels of stiffness. The stiffness of a pile relative to the surrounding soil governs the mechanisms of pile-soil interaction (Briaud *et al.*, 1984). To distinguish between relatively flexible and relatively rigid piles, criteria have been proposed by many researchers (Dobry *et al.*, 1982; Budhu and Davies, 1987; Poulos and Hull, 1989). Previous studies on laterally loaded piles were mainly concerned with the static and cyclic responses of either flexible piles (Matlock, 1970; Georgiadis, 1992; Jeanjean, 2009; Khemakhem *et al.*, 2012; Wang *et al.*, 2015) or rigid piles (Mayne *et al.*, 1995; Zhang *et al.*, 2011; Haiderali *et al.*, 2015; Murali *et al.*, 2015), as summarised in Table 1, in which the relative pile-soil stiffness for each case was calculated using Poulos and Hull's (1989) criterion.

While the lateral behaviours of flexible and rigid piles are well known, the performance of a semi-rigid pile which has a relative pile-soil stiffness between a flexible pile and a rigid pile, is rarely reported in the literature. Conceptually, semi-rigid piles may behave as either flexible piles or rigid piles, depending on the change in soil stiffness during cycling. To date, there is still a lack of understanding of the cyclic response of and soil flow mechanism around a semi-rigid pile. Therefore, the suitability of the commonly used method for designing a laterally loaded

semi-rigid pile (i.e., using p - y curves suggested by API (2007)), which was derived from field tests of flexible piles (Matlock, 1970), remains unknown.

To resist the increasingly severe cyclic loadings due to the growing capacity of onshore and offshore structures, it is common for engineers to increase the diameter throughout the entire length of the pile, although most of the lateral loading should have been resisted by the soil at shallow depths (Poulos and Davis, 1980; Randolph, 1981; Budhu and Davies, 1988; Gao *et al.*, 2015; Ng *et al.*, 2001; Reese and Van, 2001). A more economical way than using large diameter piles was proposed by Wang *et al.* (2015). They suggested strengthening only a localised area of soil surrounding a pile at shallow depths using jet-grouting. Despite the proven effectiveness of jet-grouting in reducing cumulative lateral pile displacement, the mechanism of soil flow (reflecting the area in which soil resistance is mobilised) around the jet-grouting-reinforced pile is still not well understood.

Considering the increasing demand for semi-rigid piles and jet-grouting-reinforced piles and the lack of knowledge on their lateral behavior, this study aims to understand the cyclic response of and soil flow mechanisms around a semi-rigid pile and a jet-grouting-reinforced pile. To achieve these objectives, centrifuge model tests were carried out to simulate a semi-rigid pile and a jet-grouting-reinforced pile (in soft clay) subjected to lateral cyclic loadings. Additional half-model tests were also performed for the two types of piles installed against a transparent window to continuously capture the mechanism of soil flow around the cyclically loaded piles. Supplementary finite element analyses (using an

advanced hypoplastic clay model) were performed to reveal the three-dimensional soil flow mechanism around the semi-rigid pile and to benchmark the soil flow mechanisms around a flexible and a rigid pile. Suitability of the commonly used API (2007) code for predicting the cyclic behaviours of the semi-rigid pile was also assessed.

Centrifuge modelling

All of the centrifuge model tests reported in this study were carried out at a centrifugal acceleration of 40 g in the geotechnical centrifuge facility at the Hong Kong University of Science and Technology (HKUST). The centrifuge has an effective radius of approximately 4.2 m and can operate at up to 150 g with a maximum payload of 400 g-t.

Test objective and programme

The test programme consisted of two series of tests, including three tests for semi-rigid piles and two tests for jet-grouting-reinforced semi-rigid piles. It is well recognised that one-way cycling leads to larger cumulative pile head displacement than two-way cycling at a given cyclic amplitude (Haiderali *et al.*, 2015), while the latter causes more significant bending moment than the former (He *et al.*, 2016). Since the failure of a laterally loaded pile is usually related to excessive lateral displacement instead of structural damage, one-way cycling was adopted in each cyclic loading test reported herein to simulate the worst-case scenario that produced the maximum lateral displacement of pile.

Only one-way cycling was imposed in each cyclic loading test, since it has been

found to produce a larger cumulative pile head displacement than two-way cycling

The first test series (on semi-rigid piles) included an undrained monotonic lateral loading test (Test 1) and two cyclic loading tests (Tests 2 and 3). Test 1 was performed to determine the ultimate lateral capacity (F_u) of the pile. Based on the measured F_u , representative cyclic magnitudes were determined for Test 2, in which three successive episodes of repeated lateral loading (cyclic magnitudes=15-30%, 15-45% and 15-60% F_u) were imposed on the single pile. Each episode included 100 cycles and reconsolidation was allowed between each episode of cycling. A degree of consolidation of 90% (determined from pore pressure measurements) was achieved, prior to the application of the subsequent episode. The same cyclic loading procedures were repeated in Test 3, in which a half-pile model was installed against the transparent window of the model box to reveal the mechanism of soil flow around the cyclically loaded pile. Magnitude of each episode of cycling applied to the half model pile in Test 3 was 50% of that applied in Test 2.

The second test series included two cyclic loading tests, with one test on a full jet-grouting-reinforced pile in the middle of the model box (i.e., Test 4) and the other test on a half pile installed against the transparent window of the box (i.e., Test 5). The objectives of the former and latter tests were to understand the cyclic responses of and the soil flow mechanisms around the jet-grouting-reinforced pile, respectively. In each test, three successive episodes of lateral cyclic loadings were applied to the jet-grouting-reinforced pile, with reconsolidation occurring between each episode. The procedure and magnitude of the cyclic loadings applied to the full-model and

half-model jet-grouting-reinforced piles (i.e., in Tests 4 and 5) were identical to those adopted for the full-model and half-model semi-rigid piles (i.e., in Tests 2 and 3) for ease of comparison.

Table 2 summaries the centrifuge test programme in this study, as well as the objective of each test.

Centrifuge model package

Fig. 1(a) shows the plan view of the centrifuge model package. As illustrated, five model piles (corresponding to the five tests as summarised in Table 2) were tested in one model box, which had a plan area of 14×50 m in prototype. Full model piles (in Tests 1, 2 and 4) were installed in the middle of the model box, while a half semi-rigid pile and a half jet-grouting-reinforced pile (in Tests 3 and 5, respectively) were placed against the transparent window. Through the transparent window, the mechanisms of soil flow around the two half model piles (in Tests 3 and 5) were recorded in-flight by two digital cameras. Each digital camera had a maximum resolution of 2582×1944 pixels and was fixed approximately 450 mm in front of the transparent window.

The outer diameter (D) of the semi-rigid pile was 0.8 m in prototype. The horizontal spacing between each pile was designed to be no less than $13 D$, which exceeds the major influence distance ($10 D$) around a laterally loaded pile in soft clay (Chen and Poulos, 1993).

Fig. 1(b) is a photo showing the elevation view of the model box. The soil model consisted of two strata, i.e., a 450 mm thick (18 m in prototype) soft clay underlain with a layer of medium dense sand (thickness=2 m in prototype). The single and

jet-grouting-reinforced piles were embedded to the same depth, i.e., 13.2 m in prototype. In other words, floating piles were simulated in this study and the lateral resistance to each pile was solely provided by the soft clay.

Two linear variable differential transformers (LVDTs) were used for measuring ground surface settlement, so as to deduce the degree of consolidation of the clay. To understand and compare the cyclic response of pore water pressure adjacent to the semi-rigid and jet-grouting-reinforced piles, pore water pressure transducers (PPTs) were installed in the clay on the passive side (where the lateral earth pressure increased during the cycling) of the piles in Tests 3 and 5.

Servo-controlled cyclic loading system

The monotonic or cyclic loading in each test was applied through a servo-controlled hydraulic actuator, as shown in Fig. 2(a). A load cell and an LVDT were attached to the actuator rod to provide feedback to the closed-loop system in each load-controlled test and to measure the lateral pile head displacement, respectively. The hydraulic actuator was mounted on a rigid frame, which was movable to fit the locations of the five piles tested in this study. The model pile and the cyclic loading system were connected through a rotational adapter (see Fig. 2(b)), which only constrained the lateral displacement at the pile head but otherwise allowed the free rotation and vertical movement of the pile.

Model pile

Each single model pile was made of a 420 mm long cylindrical aluminum tube (with an elastic modulus of 72 GPa). The tube had an outer and an inner diameter of

19 and 17 mm, respectively. The model piles in the cyclic loading Tests 2 and 4 were instrumented with 13 levels of foil-type strain gauges for measuring cyclic bending moments in the single pile and the jet-grouting-reinforced pile subjected to repeated lateral loading, respectively. Each level comprised four strain gauges, which were arranged as a full Wheatstone bridge to eliminate the effects of temperature variations on the measured bending moment. After installing the strain gauges, an epoxy coating (with an elastic modulus of 2 GPa) was uniformly applied on the external surface of each instrumented pile to protect it from water and moisture. The final outer diameter of the model pile (including thickness of the epoxy coating) was 20 mm. Taking into account the epoxy coating, the flexural stiffness of each pile was 195 Nm^2 , which is equivalent to 50 MNm^2 in prototype.

In the calibration of the strain gauges, each instrumented model pile was horizontally laid as a simply supported beam, with roller supports at the two ends. A vertical point load was incrementally applied at varying locations of the simply supported beam to obtain the relationship between the induced bending moment and output voltage. Satisfactory linearity (coefficients of determination R^2 no less than 0.95) was obtained for each level of strain gauges in the two instrumented piles, increasing the confidence in the measured bending moment and the p - y responses deduced from the measurement.

The relative soil-pile stiffness can be represented by a non-dimensional term $\frac{E_p I_p}{E_s l_L^4}$ ($E_p I_p$, E_s and l_L denote the flexural rigidity of the pile, soil modulus and embedded depth of the pile, respectively), as proposed by Poulos and Hull (1989). He

(2016) found that E_s of kaolin clay is equal to about 400 times its undrained shear strength (s_u), which was measured to be 10 kPa at the mid-height of the pile (details given later), the relative soil-pile stiffness parameter $\frac{E_p I_p}{E_s I_L^4}$ was calculated to be 0.0067. This value is larger than the upper bound (0.0025) for a flexible pile but smaller than the lower bound for a rigid pile (0.208) as defined by Poulos and Hull (1989). The lateral response of the piles simulated in this study, therefore, might differ from those of rigid and flexible piles.

Model grouting

It can be very difficult to simulate in-flight jet-grouting improvement in the centrifuge modeling (i.e., mixing pressurised cement slurry with clay at 40g). This is not only due to the challenging in-flight modelling technique, but also because various scale effects regarding the complex wet mixing process should be properly considered. Lee *et al.* (2006) derived the scaling relationships relevant to wet mixing of cement slurry and soil in a centrifuge. They found that the scaling related to viscosity (featured by the Reynold number), which governs the wet mixing between the cement slurry and the clay, cannot be satisfied in the centrifuge. On the other hand, the relationships regarding the significant forces involved in the wet mixing process (i.e., inertial, gravity and buoyancy forces) can be satisfied using the centrifuge modelling.

It was therefore decided not to simulate the complex in-flight mixing process of jet-grouting in this study. Instead, each model grouting was pre-cast (by mixing kaolin

clay slurry with cement) as a block in a mould and cured at 1g for 1 day, before being firmly glued to the model pile and installed into clay bed under the normal gravity. This simplified method (simulating jet-grouting as “wished-in-place”) was routinely practiced in centrifuge modelling (Kitazume *et al.*, 2001; Inagaki *et al.*, 2002). For the “wished-in-place” jet-grouting (in solid phase), the scaling relationships were mainly concerned with two parameters, namely its geometry and strength, which can be easily satisfied in the centrifuge.

It has been well recognised that the strength of soil-cement mixture in the field may be several times less than that obtained in the laboratory by mixing the same relative amounts of soil and cement (Nishida *et al.*, 1996), owing to non-uniform mixing in the field. In other words, the beneficial effects of jet-grouting improvement revealed from the centrifuge tests reported herein may represent the best-case scenario that can be achieved in the field.

As shown in Fig. 1(a), the inner and outer diameters of each model grouting were 20 and 42 mm (0.8 and 1.68 m in prototype), respectively. The depth of the grouting was determined to be $7.5 D$ (6 m in prototype), considering the lateral load applied to a pile is predominately resisted by the soil within 5 to $10 D$ below the ground surface (Poulos and Davis, 1980; Randolph, 1981; Reese and Van, 2001; Wang *et al.*, 2015). The ratios between cement, water and soil are 1: 1.6: 0.7 by mass. While pre-casting the model jet-grouting, three cubic samples ($100 \times 100 \times 100$ mm) of the clay-cement mixture with the corresponding water content, cement ratio and curing period were also prepared. The average unconfined compression strength of the three samples was

3.4 MPa, with the maximum percentage of 20%. The model grouting was prepared with sufficient strength, so as to prevent cracking in the grouting to simplify subsequent analyses.

Model preparation

Prior to the preparation of the sand and clay strata, a drainage layer made of a geotextile was placed at the bottom of the model box. The drainage layer was connected to a water tank outside the model box. Vertical drainage pipes made of the same geotextile (where the length of each drainage pipe was equal to the depth of the model box) were also installed at the four corners inside the model box. By doing so, the total water head at the top and bottom of the soil sample can be simultaneously controlled by the water tank. To minimise the friction between the transparent window and the half pile model, and the friction at the interface between the soil and the model box, silicon grease was applied to each lateral boundary inside the model box. With the presence of grease at the interface, the frictional coefficients at the pile-wall and the soil-box interfaces were found to be both smaller than 0.02 (i.e., friction angle $<1.1^\circ$), as reported by Wang *et al.* (2014) based on a series of direct shear box tests.

The bottom sandy layer (target thickness=50 mm) was then prepared by the “air pluviation” method (Ueno, 1998), i.e., sprinkling Toyoura sand into the model box at a constant falling height of 500 mm. The resulting relative density of the sandy layer was 67%. After reaching the target sandy layer thickness, the sand was saturated by connecting the bottom drainage layer to the water tank, in which the water head was

kept slightly higher than that in the sandy layer to prevent piping of sand.

The clay adopted in the centrifuge tests was reconstituted from Speciwhite China Kaolin clay with a liquid limit (LL) of 61%, plastic limit (PI) of 27% and a specific gravity of 16.5kN/m³. The dry clay powder was mixed with de-ironed water (at twice the LL of the clay, i.e., 120%) and de-aired in a vacuum mixer for about 6 hours. The fully saturated slurry was then carefully poured into the model box to form an 800 mm thick clay layer.

The slurry was consolidated in two stages, i.e., preliminary consolidation at 1g, followed by in-flight consolidation at 40g. During preliminary consolidation, the clay surface was fully covered by a rigid plate made of steel. Deadweight was incrementally applied to the rigid plate, resulting in surcharge loadings of 1, 5, 10, 15 and 20 kPa on the clay surface. Each loading increment was applied only after settlement of the rigid plate caused by the preceding surcharge loading had stabilised.

Upon completion of preliminary consolidation at 1g, the surface surcharge was removed and the model box was transferred to the centrifuge for in-flight consolidation (under the soil sample's own weight) at 40g. Throughout the in-flight consolidation, the water table was maintained at about 10 mm above the ground surface to ensure a full saturation of the soil sample. Based on the consolidation settlements measured by the two LVDTs (see Fig. 1 (b)), the degree of consolidation of the clay bed was estimated using the method proposed by Tan *et al.* (1991). The target degree of consolidation in each in-flight consolidation test was 90%, which is likely to signify the completion of primary consolidation (Terzaghi, 1943). The

consolidation settlements measured by the two different LVDTs (horizontal spacing between each was about 400 mm) differed by no more than 8%, suggesting a reasonable uniformity of the clay bed. An in-flight T-bar penetrometer test was then performed for strength characterisation (to be presented in the following section).

After in-flight characterisation of shear strength, the centrifuge was spun down for installing model piles and pore pressure transducers at 1g. During the 1g installation, each model pile was rigidly connected to an actuator, before being vertically driven into the clay bed. After installing the piles and transducers, the centrifuge model package was spun up to 40g for re-consolidation. During the re-consolidation, some negative skin friction and positive skin friction would have been developed along the upper and lower portion of the pile shaft, respectively (Lam *et al.*, 2008). Similar equilibrium process was anticipated to occur in the field, during the re-consolidation following the in-situ pile driving. After the equilibrium of the soil profile in the centrifuge, as indicated by dissipation of excess pore pressures measured around the pile, lateral monotonic or cyclic loading test of each pile was commenced.

Characterization of the undrained shear strength of the clay stratum

At 40g, the distribution of over-consolidation ratio (OCR) of the clay with depth can be readily deduced, as shown in Fig. 3(a). The clay bed was normally consolidated (OCR=1), except the soil near the ground surface (0 to 3 m below the surface).

The undrained shear strength of the clay was characterised in-flight by a T-bar penetrometer which was 6.5 mm in diameter and 35 mm in length. According to

Stewart and Randolph (1991), to ensure undrained shearing during the T-bar penetration process, the penetration rate (v) should satisfy the following relationship:

$$v > \frac{20C_v}{B} \quad (1)$$

where B and C_v represent the diameter of the T-bar penetrometer and the vertical consolidation coefficient of kaolin clay (i.e., 3×10^{-7} m²/s), respectively. According to Equation (1), the undrained penetration rate of the T-bar should exceed 0.9 mm/s. A penetration rate of 1 mm/s was therefore adopted in this study.

Fig. 3(b) shows the measured undrained shear strength (s_u) of the clay. s_u profiles calculated from two semi-empirical equations (Bolton and Stewart 1994; Gourvenec *et al.* 2009) for kaolin clay are also shown in the figure for comparison. It can be seen that the measured s_u profile is mainly bounded by the two calculated profiles, with an average value of 10 kPa at the mid-height of the pile.

Interpretation of the measured test results

In the following sections, all results are interpreted in prototype scale, unless stated otherwise.

Monotonic load-displacement response

Fig. 4 shows the measured monotonic load-displacement response at the head of the semi-rigid pile, which serves as a basis for determining the ultimate lateral capacity of the pile (F_u). In this study, the lateral capacity of the pile is determined based on the method proposed by Kulhawy and Chen (1995). In their method, it is suggested to fit the measured relationship between the lateral load (F) and the

resulting lateral pile head displacement (δ_h) with the following hyperbolic curve:

$$F = \frac{\delta_h}{a + b\delta_h} \quad (2)$$

where a and b are two fitting parameters. The reciprocals of a and b represent the interpreted ultimate lateral capacity and initial pile head stiffness, which are 221kN and 1970 kN/m for the semi-rigid pile, respectively.

In the same figure, the calculated load-deflection relationships based on some existing p - y curves (Georgiadis *et al.* 1992, API 2007, Jeanjean 2009), which were deduced from experiments of flexible piles in clay, are also included in the figure for comparison. The calculation was performed in the finite element program ABAQUS (Systèmes, 2007), in which a beam was constructed on an elastic foundation model, with consideration of various existing p - y curves for the elastic foundation. As illustrated, the initial stiffness of the measured load-deflection responses is larger than the responses calculated using the p - y curves proposed by API (2007) and Georgiadis *et al.* (1992), but smaller than that calculated with Jeanjean's (2009) p - y curves. It is worth noting that the measured maximum lateral capacity (when $\delta_h/D=0.9$) of the semi-rigid pile is smaller than that estimated using all three existing methods (Georgiadis *et al.* 1992, API, 2007, Jeanjean 2009). An explanation for this is given in the section "Mechanism of soil flow around the pile".

Cyclic load-displacement response

Fig. 5 shows the measured relationship between the cyclic loading and the resulted normalised pile head displacement (δ_h/D) during the three successive episodes of one-way loading (cyclic magnitudes=15-30%, 15-45% and 15-60% F_u).

The measured monotonic load-displacement curve is also included for comparison. It can be seen that the stiffness degradation and cumulative pile head displacement increased with number of cycles and cyclic magnitude. During the initial loading cycle in each of the three cycling episodes, the load-displacement relationship closely followed the virgin monotonic push-over response. This implies that the cyclically remolded clay adjacent to the pile had re-gained stiffness during the re-consolidation between each episode of cycling. Probably due to the re-consolidation, the load-displacement response during the initial cycle in the 3rd loading episode (cyclic magnitudes=15-60% F_u) even exhibited a slightly higher stiffness than the virgin monotonic response.

Similar observations were also made by Jeanjean (2009) based on a series of centrifuge tests simulating piles subjected to lateral cyclic loading in lightly over-consolidated kaolin clay. It was reported by Jeanjean (2009) that small amplitude load cycles (cyclic amplitude up to 54% F_u) did not seem to have any negative influence on the subsequent cyclic or monotonic load-displacement response, given reasonable soil consolidation was allowed between the loading episodes. Unlike the test resulted reported herein and by Jeanjean (2009), Zhang *et al.* (2011)'s centrifuge tests shown that re-consolidation of soft clay after very large amplitude of lateral displacement cycling (cyclic magnitude= $\pm 0.5 D$) can only lead to a 70% recovery in the lateral pile stiffness. The afore-mentioned comparisons may suggest that the lateral pile behaviour can be either fully or partially recovered by re-consolidation, depending on the degree of cyclic remolding during the preceding loading episode.

Accumulation of cyclic lateral pile head displacement

Fig. 6(a) shows the measured development of lateral displacement at the head of the semi-rigid pile during the three episodes of one-way cycling (cyclic magnitudes=15-30%, 15-45% and 15-60% F_u). It can be seen that at any given load cycle, the lateral pile head displacement (δ_h) is comprised of a recoverable elastic component (δ_{he}) and an irrecoverable plastic component (δ_{hp}).

During the small amplitude of cycling (i.e., the first loading episode with cyclic magnitude of 15-30% F_u), the elastic displacement δ_{he} remained almost constant while the plastic displacement δ_{hp} increased with the number of cycles at a decreasing rate, i.e., it was a shakedown response (Swane and Poulos, 1982, Hu *et al.*, 2012). δ_{hp} stops increasing after 65 loading cycles. At the last cycle of the first episode, 82% of the total lateral pile head displacement was irrecoverable ($\delta_{hp}/\delta_h = 82\%$). When subjected to the second episode of cycling at an elevated loading magnitude (compared to that in the first episode), δ_{he} and δ_{hp} evolved according to similar trends (i.e., a shakedown response) to those resulting from the first episode of cycling, but at a larger magnitude. At the last loading cycle, the irrecoverable lateral pile head displacement accounted for 80% of the total ($\delta_{hp}/\delta_h = 80\%$), which is similar to that due to the first episode of cycling. During the third episode of loading with the largest cyclic magnitude (15-60% F_u), the plastic lateral pile displacement δ_{hp} increased almost linearly with the number of cycles, suggesting a consistent increase in energy dissipation at every cycle (i.e., ratcheting pattern). Despite the linear increase in δ_{hp} with loading cycle, the magnitude of the elastic component δ_{he} remained constant during the 100 cycles in

the third episode. At the 100th loading cycle of the third episode, 90% of the total lateral displacement was irrecoverable ($\delta_{hp}/\delta_h=90\%$).

Fig. 6(b) shows the measured cumulative lateral displacement at the head of the jet-grouting-reinforced pile, as a result of three episodes of one-way cycling. Cyclic magnitudes of the three episodes were 15-30%, 15-45% and 15-60% F_u , which were identical to those applied to the semi-rigid pile for comparative purpose. The jet-grouting-reinforced pile exhibited a shakedown response to all three episodes of loading. A comparison between Fig. 6(a) and Fig. 6(b) suggests that by applying jet-grouting around the semi-rigid pile at shallow depth (depth of grouted zone = 7.5 D), the maximum lateral pile head displacement was reduced by 80, 83 and 90% during the first, second and third episodes of cycling, respectively. In addition, the maximum value of δ_{hp}/δ_h of the jet-grouting-reinforced pile (i.e., 68%) was much smaller than that of the semi-rigid pile. This implies that application of jet-grouting reduced soil yielding around the pile, and consequently the proportion of irrecoverable lateral displacement of the pile.

To generalise the cumulative trend of the measured lateral pile displacement for future predictions, it is a usual practice to establish the relationship between the normalised pile head displacement $\delta_{h-n}/\delta_{h-1}$ and the number of cycles N (Khemakhem *et al.*, 2010). The terms δ_{h-1} and δ_{h-n} denote the lateral pile head displacement at the 1st and the n^{th} loading cycle. Fig. 6(c) and Fig. 6(d) show the measured and curve-fitted relationships between $\delta_{h-n}/\delta_{h-1}$ and N for the semi-rigid pile and the jet-grouting-reinforced pile, respectively. The shakedown responses (due to the first

two loading episodes of the semi-rigid pile, and all three loading episodes of the jet-grouting-reinforced pile) can be well fitted by an exponential function. On the other hand, the ratcheting pattern (resulting from the third loading episode of the semi-rigid pile) has to be fitted by a linear function, as anticipated.

Cyclic pore water pressure response

The cyclic accumulation of plastic lateral pile displacement in clay, as discussed in the preceding section, is likely related to irrecoverable pore water pressure accumulated during the cyclic loading. Fig. 7(a) shows the development of pore water pressure in front of the semi-rigid pile, as a result of the three episodes of lateral cycling. The pore water pressure was measured at a distance of $1D$ in front of the pile, and at a depth of $3D$ below the ground surface, where the initial over-consolidation ratio was about 1.3. In the figure, the excess pore water pressure (Δu) is normalised by the initial vertical effective stress (σ'_v) at the corresponding location.

As expected, positive excess pore water pressure was generated in the lightly over-consolidated clay during each episode of cycling. At any given loading cycle in each episode, the total excess pore water pressure was composed of an elastic component (Δu_e) and a plastic component (Δu_p). The presence of Δu_p implies development of plastic strain in the soil, which led to the irrecoverable lateral pile head displacement (δ_{hp} , see Fig. 6).

In response to the first two loading episodes, the excess pore pressure accumulated but at a decreasing rate during the initial 60 cycles of repeated shearing. This was followed by a slight reduction in pore water pressure likely caused by

consolidation. The progressively stabilised pore water pressure responses are in line with the shakedown responses of the lateral pile head displacement during the first two episodes of cycling, as shown in Fig. 6(a). In contrast, a continuous accumulation of irrecoverable pore pressure (Δu_p) was registered in front of the semi-rigid pile during the third episode of cycling, with the maximum normalised pore pressure $\Delta u_p/\sigma'_v$ being equal to 0.4. This rapidly accumulated pore pressure had likely significantly softened the soil around the pile, leading to the ratcheting pattern of the cyclic pile head displacement (Fig. 6(c)).

Fig. 7(b) illustrates the normalised cyclic pore water pressure ($\Delta u/\sigma'_v$) in front of the grouting-reinforced pile during the three episodes of cycling. The location of the pore pressure measurement in this case corresponded to the front of the semi-rigid pile (i.e., at a depth of $3D$ and a distance of $1D$ in front of the pile). A progressively stabilised response was measured in response to all three loading episodes with increasing cyclic magnitude. This is consistent with the shakedown responses of the lateral pile displacement during the three episodes of cycling.

A comparison between Fig. 7(a) and Fig. 7(b) shows that, by applying jet-grouting around the semi-rigid pile, the elastic and plastic cyclic pore pressures were greatly reduced, with a maximum percentage reduction of 75%. This suggests that the presence of the jet-grouting had alleviated the cyclic degradation of soil around the pile, and consequently significantly reduced the cumulative lateral pile displacement (see Fig. 6(a) and Fig. 6(b)).

Evolution of pile deformation mode with cycling

Since the cumulative cyclic pore water pressure gradually degraded the soil stiffness around the pile, the relative pile-soil stiffness should have been altered, causing a potential change in the deformation mode of the pile. Figs. 8(a), 8(b) and 8(c) show the measured lateral deformation profiles of the two types of piles (based on PIV analyses of Tests 3 and 5) resulting from the first, second and third episodes of lateral repeated loading, respectively. For clarity, each figure only includes pile deformation induced by three typical loading cycles (1st, 50th and 100th cycle). In addition to the lateral deformation, each figure also shows the maximum rotation angle at the head of each type of pile, which is a key parameter determining the serviceability of the high-rise superstructure.

All three figures show that during each episode of cycling, the semi-rigid pile initially (i.e., 1st cycle) deformed as a flexible pile. As the number of loading cycles increased (i.e., 50th and 100th cycle), which softened the soil due to the cumulative plastic strain (as implied by irrecoverable pile displacement in Fig. 6(a)) and accumulated cyclic pore pressure (Fig. 7), the pile tended to behave as a rigid pile, i.e., rotating without significant flexure. The location of the rotation point shifted upwards, from a depth of $0.9 L$ (L =pile embedment depth) at the end of the first episode of cycling, to $0.78 L$ on completion of the third loading episode. On the other hand, the jet-grouting-reinforced pile behaved as a rigid pile throughout the three episodes of cyclic loading.

According to Achmus *et al.* (2009), the maximum allowable rotation (at the

ground surface) of a pile supporting a wind turbine should not exceed 0.5° during the entire operating period. If this criterion (i.e., rotation $< 0.5^\circ$) were adopted, then the measured pile head rotations at the end of each cycling episode would suggest that the semi-rigid pile may only be allowed to sustain a cyclic magnitude of up to $0.3 F_u$, while the jet-grouting-reinforced pile may be able to sustain a cyclic magnitude exceeding $0.6 F_u$.

While subjected to the largest magnitude of cyclic loading (i.e., third episode of cycling), the induced maximum rotation and lateral displacement at the head of the jet-grouting-reinforced pile were only 10 and 17% of those of the semi-rigid pile, respectively. The effectiveness of jet-grouting in reducing cumulative pile rotation and deformation under cyclic loading was thus well demonstrated.

Mechanism of soil flow around the pile

The evolution of the deformation mode of the semi-rigid pile with cycling likely altered the soil flow mechanisms around the pile. Figs. 9(a), 9(b) and 9(c) illustrate the measured soil flow mechanisms in the vertical symmetrical plane of the pile, caused by the 1st, 50th and 100th loading in the third episode of cycling (cyclic magnitude = 15-60% F_u), respectively. Due to the 1st cycle of lateral loading, which caused flexural deformation of the pile (see Fig. 8(c)), the soil flow mechanism consisted of a wedge mechanism near the ground surface (0 to 3.5 m below the surface) and horizontal soil flows (i.e., a full-flow mechanism in the horizontal plane, as revealed later by the numerical analysis) at greater depth. This experimental evidence supports the soil flow mechanisms (i.e., a wedge mechanism near the

surface and a full-flow mechanism at greater depth) hypothesized by Klar & Randolph (2008), while deriving their upper-bound solution for a laterally loaded flexible pile.

As the number of loading cycles increased, which gradually altered the deformation mode of the semi-rigid pile (from flexural mode to rotational mode, see Fig. 8(c)), a rotational soil flow mechanism was formed near the lower half of the pile as shown in Figs. 9(b) and 9(c). Additionally, a gap was developed behind the pile. Three distinct soil flow mechanisms can be identified at the end of the third episode of cycling, namely a wedge mechanism near the surface, horizontal soil flows near the middle of the pile, as well as rotational soil flows at the lower half of the pile.

Figs. 10(a), 10(b) and 10(c) show the measured soil flow mechanisms in the vertical symmetrical plane of the jet-grouting-reinforced pile subjected to the 1st, 50th and 100th loading during the third episode of cycling. Differing from the semi-rigid pile, the predominating soil flow mechanism around the jet-grouting-reinforced pile was solely a wedge-type mechanism, which originated from a depth of 6 m (equal to the depth of the jet-grouting) and extended to the ground surface. This wedge-type mechanism was not altered with the increasing loading magnitude during the entire cycling process. In other words, the three episodes of cyclic loading (cyclic magnitude=15-60% F_u) can be sufficiently resisted by mobilising soil resistance around the jet-grouted portion of the pile (which enlarges the apparent diameter of the pile), with no need to transfer the lateral head load downwards to a greater depth. It is also worth noting that the presence of the jet-grouting helped prevent the formation of

unfavorable gapping behind the grouted pile.

Cyclic bending moment profile

Fig. 11 shows the bending moment profiles of the semi-rigid pile and the jet-grouting-reinforced pile after the 1st, 50th and 100th lateral loading during the third episode of cycling (cyclic magnitude = 15-60% F_u). As can be seen, the bending moment of the semi-rigid pile increased with the number of cycles, as the soil around the pile progressively softened due to the cumulative plastic strain (as implied by Fig. 6(a)) and excess pore water pressure (see Fig. 7(a)). In the meantime, as the number of loading cycle increased, the location of the maximum bending moment moved downwards from a depth of 5 m to 6 m below the ground surface. This was because of the downward lateral stress transfer along the pile. In other words, cyclic degradation of soil resistance at shallow depths facilitates mobilisation of resistance at deeper depths to maintain horizontal equilibrium. The maximum bending moment (due to the application of the 100th cycling) was measured to be 776 kNm, which is equivalent to 97% of the yield moment of a reinforced concrete pile with an outer diameter of 0.8 m at zero axial load (i.e., 800 kNm, as estimated by Loganathan *et al.* (2000)).

By applying jet-grouting around the semi-rigid pile at a shallow depth, the maximum bending moment at each given number of cycling was greatly reduced, with a maximum percentage reduction of 45%. In addition, the location of the maximum bending moment (about 6 m below the ground surface) did not change throughout the entire cycling process. This implies that the cyclic loading can be sufficiently resisted by mobilising soil resistance around the jet-grouted region (depth

ranging from 0 to 6 m below the surface), without a need for downward lateral load transfer. A similar conclusion has been made independently by interpreting the soil flow mechanism around the jet-grouting-reinforced pile, as discussed in the preceding section.

Cyclic p - y response

Based on the measured bending moment profile and the lateral pile deflection (y) of the semi-rigid pile, cyclic p - y responses can be deduced. Fig. 12 shows the deduced cyclic p - y curves at three typical depths (4, 7, and 10 D below the ground surface), where distinctively different soil flow mechanisms were developed. The p - y response due to the 3rd episode of cycling (cyclic magnitude = 15-60% F_u) was not included in the figure, because the pore pressure kept accumulating in this loading episode (Fig. 7(a)). In other words, Fig. 12 only shows the final stable p - y responses resulting from the 1st and 2nd episodes of cycling.

The soil reaction force (p) shown in the figure was obtained by taking the second derivative of the maximum bending moment profile (which was best-fitted by a sixth-order polynomial) measured at every 20 cycles in Test 2 (full-pile model test). The lateral pile displacements (y) at the three selected depths were measured based on the PIV analyses of the images taken at the same loading cycles in Test 3 (i.e., half-pile model test). Since the cumulative pile head displacements in Test 2 (measured by LVDT) and Test 3 (measured by PIV analysis) were quantitatively comparable (maximum percentage difference between the two smaller than 17%), the lateral pile displacements at different depths measured in Test 3 were representative of

those resulting from the same cyclic loading in Test 2.

Figs. 12(a), 12(b) and 12(c) show the deduced cyclic p - y responses at the three typical depths. For comparison, the cyclic p - y curves recommended by the API (2007) code, which was developed based on field test results of a cyclically loaded flexible pile, are also included in the figure. At the chosen depths where a wedge mechanism and a full-flow mechanism ($4 D$ and $7 D$ below the surface) dominated, the deduced cyclic p - y curves show larger initial stiffness and ultimate bearing capacity factor than those suggested by API (2007). Similar observations were reported by Steven & Audibert (1979), Hamilton *et al.* (1991) and Jeanjean (2009), based on the comparison between the API and the deduced p - y curves from their experiments of flexible piles in soft clay. By underestimating the initial stiffness and ultimate bearing capacity factor, the API (2007) code is like to give conservative predictions.

On the contrary, the API (2007) code significantly overestimated the ultimate bearing capacity factor near the lower half of the pile (signified by the p - y at a depth of $10 D$, see Fig. 12(c)) by 52%. This was likely because the code (2007) assumed a full-flow mechanism at depth with a constant bearing capacity factor of 6.5, while the rotational soil flow mechanism was actually formed near the lower half of the semi-rigid pile (Fig. 9(c)). The reason that the rotational soil flow mechanism is associated with a lower bearing capacity factor than the full-flow mechanism is explained in the section “Preliminary finite element analyses”. Probably because of the same reason, the measured maximum lateral capacity of the semi-rigid pile was smaller than that estimated using all the p - y curves derived from flexible piles, as

observed in Fig. 4.

Assessing validity of API's cyclic p - y curves for predicting lateral deformation and bending moment

Based on the measured cyclic lateral pile displacement (Fig. 8) and bending moment (Fig. 11) in this study, it is worth assessing the validity of the cyclic p - y curves suggested by API (2007) for predicting the behaviour of a semi-rigid pile. To achieve this objective, the resistance-deflection relationships recommended by the code are incorporated into a beam on the elastic foundation model, which was constructed in the finite element program ABAQUS. Thirteen levels of nonlinear springs were assigned along the depth of the semi-rigid pile, with a vertical spacing of 1 m between each spring. A lateral load of 128 kN, which was equal to the cyclic magnitude adopted in the third episode of cycling in the test, was applied at the pile head. In the calculation, the possible change in undrained shear strength of the reconsolidated clay following the first two cycling episodes was not taken into account.

Fig. 13(a) shows the measured and calculated profiles of lateral pile displacement due to the 1st, 50th and 100th loading during the third episode of cycling. The calculated lateral pile displacement based on the static p - y curves of the API code corresponded to the measured profile under the 1st loading cycle. Meanwhile, the deformation profile calculated using the cyclic p - y curves of the API code, which does not explicitly account for the influence of cycling number, was compared with the measured deformation profiles due to the 50th and the 100th cycling.

The result calculated using API's static p - y responses overestimated the measured lateral displacement due to the 1st loading of the pile, which deformed like a flexible pile. The overestimation was somewhat expected, since it has been found that the stiffness and strength of the static p - y curves given by API tend to be conservative (Steven & Audibert 1979; Hamilton *et al.*, 1991; and Jeanjean, 2009).

In contrast, while subjected to the 50th and the 100th cycles of lateral loading, the results calculated using API's cyclic p - y curves led to non-conservative estimation of the measured lateral displacement due to the 50th and 100th cycles of the pile, which tended to behave as a rotational rigid pile. The calculated cumulative lateral displacement and rotation at the pile head (using the code) resulting from 100 cycles of lateral load were only 31% and 40% of the measured data, respectively. This is because the API code (2007), which assumes a full-flow mechanism at depth with a constant bearing capacity factor of 6.5, overestimated the actual resistance factor (approximately 4.2, see Fig. 12(c)) for the rotational soil flow mechanism near the lower half of the pile.

Fig. 13(b) shows the measured and the bending moment profiles resulting from the 1st, 50th and 100th loading during the third episode of cycling. The measured static bending moment (due to the 1st loading) was overestimated by the calculated profile using the API's (2007) static p - y curves. On the contrary, the measured cyclic bending moments (due to the 50th and 100th cycling) were underestimated by the calculated profile with the API's (2007) cyclic p - y curves. These trends are consistent with those observed from the comparisons between the measured and calculated lateral pile

displacements (Fig. 13(a)) for the same reasons as explained in the earlier part of this section.

In summary, the cyclic p - y curves of the API code (2007) are likely to result in a non-conservative estimation of deformation and bending moment in a cyclically loaded semi-rigid pile, as it ignores the rotational soil flow mechanism (which exhibits lower resistance than the full-flow mechanism) near the lower half of the pile.

Preliminary finite element analyses

Objective

Despite the soil flow mechanisms visualized from the half-model centrifuge tests, the transverse flow mechanisms in the horizontal planes at different depths around the piles are not available. To reveal three-dimensional soil flow mechanisms around the cyclically loaded semi-rigid pile, a numerical back-analysis of centrifuge test 2 was carried out, using a hypoplastic clay model considering the cyclic degradation effects. Apart from the back-analysis of the semi-rigid pile, two additional numerical analyses (on a flexible and a rigid pile) were performed to understand the influence of pile diameter on the soil flow mechanism, and the associated lateral soil resistance. In the additional analysis, diameters of the flexible and rigid piles were 0.3 m and 4 m, corresponding to relative pile-soil stiffness ($\frac{E_p I_p}{E_s I_L^4}$) of 0.00019 and 6.2, respectively.

As defined by Poulos and Hull (1989), the upper bound and lower bound values of

$\frac{E_p I_p}{E_s I_L^4}$ for flexible and rigid pile are 0.0025 and 0.208, respectively.

Finite element mesh and numerical modelling procedure

Fig. 14 shows an isometric view of the finite element (FE) mesh and the boundary conditions of the numerical back-analysis for centrifuge test 2 (i.e., semi-rigid pile subjected to lateral cyclic load). By taking advantage of symmetry, only half of the centrifuge model was simulated in the FE analysis. Each lateral boundary of the FE mesh was constrained by roller supports while the bottom boundary was fixed by pinned supports. Dimensions of the soil and the pile were identical to those adopted in centrifuge test 2. A gravitational acceleration of 40 g was imposed on the entire FE mesh.

Coupled-consolidation analysis was performed to simulate accumulation of excess pore water pressure, and therefore degradation of stiffness and strength of the clay around the cyclically loaded pile. During the entire process of the FE analysis, the water table was maintained at the ground surface, by imposing pore water pressures on the top and the bottom of the clay stratum with constant values of 0 and 180 kPa (equal to the initial hydrostatic pressure) throughout the analysis, respectively.

The clay and the pile were modelled using C3D8P elements (considering pore pressure response at each node of the element) and S4 shell elements, respectively. The suitability of the current mesh size (as shown in Fig. 14) was justified by halving the mesh and running one more analysis. The difference in the computed lateral pile displacements from the two analyses with different mesh sizes was no more than 3%, justifying the validity of the mesh size adopted in the present study.

The interaction between the pile and the clay was modelled by defining zero-thickness interface slip elements at their contact surfaces, so as to allow relative shear displacement between, and separation of the two objects. The frictional interface behaviour was simulated based on the Coulomb friction law, which requires two parameters, i.e., the interface friction coefficient (μ) and the limiting relative soil pile movement (γ_{limit}). According to Hong *et al.* (2014), the values of μ and γ_{limit} at the interface between kaolin clay and epoxy coating are approximately 0.3 and 5 mm, respectively. It is worth noting that pile-soil tension (due to negative excess pore pressure) at the rear of the pile was not considered in this numerical analysis. This may have led to an underestimation of the lateral soil resistance at shallow depths, and therefore an overestimation of the lateral pile head displacement.

Regarding the numerical modelling procedure, the three episodes of cyclic loading in centrifuge test 2 (cyclic magnitude=15-30%, 15-45% and 15-60% F_u) were simulated in three individual numerical runs, with one episode of cycling modelled in each run. The reason for not simulating the three successive episodes of cyclic loading in one single numerical run is because the meshes of the soil around the pile would become greatly distorted during the reconsolidation after each episode of cycling, which would increase numerical instability for the subsequent analysis.

Large-deformation technique was used in each numerical analysis (by activating the non-linear geometry option in each loading step), because relatively large lateral displacement (up to $0.8D$) and rotation (up to 3.35°) were observed in the piles under either monotonic or cyclic loading. By doing so, the deformed geometry of each

element was updated after each loading increment, to capture the significant change in the size, shape and position of the soil elements adjacent to the laterally loaded pile.

A hypoplastic model accounting for cyclic responses of clay.

A hypoplastic clay model (Mašín, 2014), which is capable of simulating cyclic responses of clay and is relatively easy to implement in numerical code, is used for the numerical analyses in this study. Mašín and Herle (2005) firstly developed a basic hypoplastic clay model, which is suitable for predicting soil responses subjected to monotonic loading at medium to large strain levels. An improvement of the model was then made by Mašín (2005) to better predict the cyclic response of soil and to improve the model performance in the small-strain range. Mašín (2014) further enhanced Mašín's (2005) model by incorporating stiffness anisotropy.

In the hypoplastic clay model adopted in this study (Mašín, 2014), the non-linear stress-strain behaviour of clay is formulated based on the theory of hypoplasticity as follows:

$$\overset{\circ}{\mathbf{T}} = f_s (\mathbf{L} : \mathbf{D} + f_d \mathbf{N} \|\mathbf{D}\|) \quad (3)$$

where $\overset{\circ}{\mathbf{T}}$ and \mathbf{D} represent the objective (Zaremba-Jaumann) stress rate and the Euler stretching tensor, respectively, \mathbf{L} and \mathbf{N} are fourth- and second-order constitutive tensors, and f_s and f_d are two scale factors. In hypoplasticity, non-linear soil behaviour is implied by the fact that the stress rate $\overset{\circ}{\mathbf{T}}$ in Equation (3) varies non-linearly with the strain rate \mathbf{D} , owing to the non-linear form given by the Euclidian norm (i.e., $\|\mathbf{D}\|$). Thus, the non-linear behaviour is predicted without a need of the yield surface.

Since the yield surface is not explicitly defined in the hypoplastic model, there is

no need to numerically distinguish between elastic and plastic regions (i.e. no conditional statements), making it relatively easy to implement the model in numerical code.

The concept of critical state soil mechanics is also incorporated in the hypoplastic clay model. To be more specific, the positions of the isotropic normal compression line and the critical state line correspond to those in the modified Cam clay model. The failure surface proposed by Matsuoka and Nakai (1974) is adopted as the limit stress criterion.

To reasonably simulate cyclic responses of clay, the intergranular strain concept (introduced by Niemunis and Herle (1997)) is incorporated into the present hypoplastic clay model. It was shown by Niemunis and Herle (1997) that the inclusion of the intergranular strain concept can effectively reduce the excessive ratcheting upon cyclic loading (or repeated strain path reversal), which is usually predicted by the hypoplastic models without referring to the intergranular strain concept. Detailed formulation of the hypoplastic clay model can be found in Mašín and Herle (2005), Mašín (2005) and Mašín (2014). The remaining part of this section mainly focuses on the description and calibration of the model parameters.

The hypoplastic clay model adopted in this study consists of 11 parameters. Five out of the 11 parameters, i.e., ϕ'_c , N , λ^* , κ^* and ν , are equivalent to those defined in the modified Cam clay model. The parameters ϕ'_c denote effective angle of shearing resistance at critical state. N , λ^* and κ^* are position of the isotropic virgin compression line, slope of the isotropic virgin compression line and slope of the

unloading line in $\ln(1+e)-\ln(p')$ space (as defined by Butterfield, 1979), respectively.

The parameter ν regulates the proportion of bulk and shear stiffness. Values of the five parameters are given in Table 3.

Apart from the five parameters controlling the monotonic behaviour of clay at medium to large strain levels, there are six other parameters governing the small-strain stiffness of clay subjected to various strain path reversals (relevant to cyclic response), i.e., R , m_{rat} , β_r , χ , A_g and n_g . The parameter R denotes the strain range of soil elasticity. The parameter m_{rat} (ranging between 0 and 1) controls the path-dependency of soil stiffness at small strains. It quantifies the ratio between initial small-strain stiffness upon a 90° strain path reversal and the initial stiffness upon a 180° strain reversal. The parameters β_r and χ control the strain-dependency (i.e., degradation rate of stiffness with strain) of soil stiffness at small strains. The remaining two parameters A_g and n_g represent the stress-dependency of small strain stiffness. The dependency of small-strain stiffness G_o on mean effective stress p' , which is a function of A_g and n_g , is formulated by Wroth and Houlsby (1985), as follows:

$$G_{ip0} = p_r A_g \left(\frac{p}{p_r}\right)^{n_g} \quad (4)$$

where A_g and n_g are parameters and P_r is a reference pressure of 1 kPa.

The parameters R , m_{rat} , β_r , χ adopted in this study follow those calibrated by He (2016) against data reported by Benz (2002) on the small-strain stiffness of kaolin clay. He (2016) found that the cyclic response predicted by the hypoplastic clay model was very sensitive to the parameters ν , A_g and n_g . Since cyclic test results of kaolin

clay are rarely available in the literature, He carried out cyclic triaxial tests. In the triaxial test, a reconstituted kaolin clay sample was consolidated under an isotropic confining stress of 200 kPa, followed by 100 cycles of undrained cyclic triaxial compression at a constant cyclic magnitude (i.e., 40% s_u of the soil specimen), which was determined by a monotonic undrained triaxial compression test on the same soil with the same initial condition. Results of the cyclic triaxial test and of centrifuge test 2 (simulating cyclic response of a pile) were then used to calibrate the parameters ν , A_g and n_g . Fig. 15 shows the measured and calibrated cyclic stress-strain relationship in the triaxial test. Comparisons between the centrifuge test results and the model predictions are given in the next section.

All of the 11 model parameters adopted in the numerical analyses reported here are summarized in Table 3. In addition to the 11 model parameters, four other parameters had to be determined: the initial void ratio (e), coefficient of lateral earth pressure (K_o), and vertical and horizontal permeability (k_v and k_h). The variation in e with depth can be readily calculated based on the known effective stress level and OCR (see Fig. 3(a)) at each depth. The distribution of K_o with depth was estimated using Mayne Kulhawy's (1982) semi-empirical equation, which is a function of ϕ'_c and OCR. The values of k_v and k_h were determined based on Al-Tabbaa's (1987) semi-empirical equations, which are functions of the void ratio.

Comparison between the measured and computed cyclic lateral pile displacement

Figs. 16 compares the measured and computed cumulative lateral displacements at the head of the semi-rigid pile (in test 2), as a result of the three episodes of lateral

cycling. Both measured and computed results show that during the first two episodes of cycling (i.e., cyclic magnitude=15-30% and 15-45% F_u), the cumulative lateral pile head displacement increased with the number of cycles but at a decreasing rate, suggesting a shakedown response. During the 3rd episode of cycling (i.e., cyclic magnitude=15-60% F_u), however, both the measured and computed cumulative lateral pile head displacements increased with the number of cycles at an almost constant rate, indicating a ratcheting pattern. Quantitatively, the computed cyclic lateral pile displacement underestimated the measured one during all episodes of cycling, with a maximum percentage underestimation of 25%.

Even though pile-soil tension (due to negative excess pore pressure) at the rear of the pile was ignored in the numerical analysis, the computed lateral pile displacement was still slightly smaller than the measured one at each episode of cycling (see Fig. 16). This may imply that the soil simulated by the hypoplastic clay model in this study behaved more stiffly than it did in the centrifuge model test.

Effect of relative soil-pile stiffness on mechanisms of soil flow around laterally loaded piles

Figs. 17(a), 17(b) and 17(c) show the computed soil flow mechanisms around the semi-rigid pile, flexible pile and rigid pile, respectively. Each figure includes not only soil flows in the vertical symmetrical plane of the pile, but also flow mechanisms in the horizontal planes (at representative depths), which cannot be visualized in a half-pile centrifuge test. The displacement vectors shown in the figures denote cumulative soil movements resulting from 100 cycles of one-way lateral loading at a

cyclic magnitude of 15-60% F_u .

It can be seen from Fig. 17(a) that in the vertical symmetrical plane of the laterally loaded semi-rigid pile, three distinct soil flow mechanisms can be identified, namely a wedge mechanism near the ground surface (Zone I), horizontal soil flow near the middle of the pile (Zone II), and rotational soil flow near the lower half of the pile (Zone III). These observations are broadly consistent with the measured soil flow mechanisms (see Fig. 9(c)) based on the PIV analyses of Test 3. The reasonable numerical predictions for the soil flow mechanisms in the vertical symmetrical plane of the pile and for the cyclic lateral pile head displacements (see Fig. 16) increase confidence in the computed transverse soil flow mechanisms in the three representative horizontal planes (planes “A-A”, “B-B” and “C-C”).

In a horizontal plane near the ground surface (i.e., plane “A-A” in zone I), cavity flow was developed in front of the semi-rigid pile, with a gap forming behind it. Near the middle of the pile, a full-flow mechanism was formed (see plane “B-B” in zone II). Near the lower half of the pile, where rotational soil flow was formed in the vertical symmetrical plane, the width of the rotational soil flow in the horizontal plane “C-C” in zone III was equal to approximately 1.2 times of the pile diameter, suggesting soil flows were confined within the area of the pile without spreading out. The rotational soil flow mechanism (along the vertical symmetrical plane) occurring at the lower half of the semi-rigid pile, as observed in this study, was different from the full flow mechanism (along the transverse plane of a pile) being commonly assumed while analysing lateral soil-pile interaction using slip line method (Broms, 1964) and

upper-bound & lower-bound theories (Randolph and Houlsby, 1984; Murff and Hamilton, 1993; Klar and Randolph, 2008).

Differing from the semi-rigid pile, the mechanism in the vertical symmetrical plane of the flexible pile (see Fig. 17(b)) was comprised of wedge-type failure near the ground surface (zone I) and predominantly horizontal soil flows below the wedge (zone II). The computed transverse soil flows in the two representative horizontal planes (planes “A-A” and “B-B”) further reveal that cavity flow was developed in the wedged zone (plane “A-A”), while full flow prevailed at greater depths (plane “B-B”). The computed mechanism (wedge failure near the ground surface and full-flow failure at depth) is consistent with the current understanding of soil flows around a laterally loaded flexible pile. This mechanism has been adopted by Murff & Hamilton (1993) and Klar & Randolph (2008) in their upper-bound analyses, although the former did not explicitly specify that the mechanism may only be applicable to flexible piles.

For a laterally loaded rigid pile (Fig. 17(c)), two distinct flow mechanisms can be identified in the vertical symmetrical plane of the pile, i.e., a wedge mechanism near the ground surface (zone I) and rotational soil flow at depth (zone II). The transverse soil flow mechanism in plane “A-A” indicates that cavity flow was formed in the wedged zone (zone I), while the flow mechanism in plane “C-C” illustrates that the width of the rotational soil flow at depth (zone II) was approximately equal to 1.2 times of the pile diameter.

A comparison between Figs. 17(a), 17(b) and 17(c) reveals that as the

diameter-to-depth ratio of the pile increased, the soil flow mechanism near the lower half of the pile was significantly altered from full flow along the transverse section of the pile to rotational flow in the vertical symmetrical plane of the pile. On the other hand, the soil flow mechanism near the ground surface (i.e., a wedge mechanism) was merely affected by the diameter-to-diameter ratio. The progressive evolution of soil flow mechanisms with pile diameter suggests that the semi-rigid pile exhibited an intermediate behaviour combining the features of soil flow around the flexible pile and the rigid pile.

Effect of relatively soil-pile stiffness on ultimate soil resistance around laterally loaded piles

The altering soil flow mechanisms with increasing pile diameter, as revealed in the preceding section, imply that the ultimate lateral soil resistance along a pile is likely to vary with its diameter. To explore the dependency of the ultimate lateral pile resistance on pile diameter, Figs. 18(a), 18(b) and 18(c) compare the computed distributions of the bearing capacity factor ($N_p = P_u / s_u D$) with depth along the flexible pile, semi-rigid pile and rigid pile, respectively. Also included in each figure is the distribution of the bearing capacity factor as recommended by the API code (2007), which is based on results of field experiments involving flexible piles. Additionally, N_p deduced from the measurement in Test 2 is included in Fig. 18(b) for validation purpose.

For the flexible pile (Fig. 18(a)), the computed distribution of N_p shows a similar trend to that recommended by the API (2007) code, i.e., N_p increasing with depth in

the shallow region (see zone I, where a wedge mechanism dominated) and then remaining constant at greater depths (see zone II, where a full-flow mechanism prevailed). Qualitatively, the computed N_p values at different depths are slightly larger than those calculated by API (2007), with a maximum percentage difference of 13%. This overestimation is possibly due to the reason that N_p in API was deduced from two-way cycling tests, which causes more strength reduction than one-way cycling, as simulated in this numerical analysis.

Different from the flexible pile, the distribution of N_p along the semi-rigid pile (see Fig. 18(b)) is much more complicated. As shown by both measured (in Test 2) and computed results, the value of N_p in the shallow region (i.e., zone I, where a wedge mechanism prevailed) increases with depth as expected. Near the middle of the pile (i.e., zone II, where a full-flow mechanism governed), however, the N_p value shows a general trend of reducing with depth. This is likely attributed to the gradual transition from a full-flow mechanism in zone II to a rotational soil flow mechanism in zone III. It is clearly illustrated in the inset of Fig. 17(b) that the area of soil in full flow mobilised in the horizontal plane “B-B” to resist lateral movement of the pile is larger than the area of rotational soil flow mobilized in the horizontal plane “C-C”, resulting in a generally higher N_p value for the former than the latter. The N_p value along the lower half of the semi-rigid pile (i.e., zone III, where a rotational soil flow mechanism dominated) shown a bilinear distribution with depth. This is different from the uniform distribution corresponding to the typically assumed full-flow mechanism (Broms, 1964; Murff and Hamilton, 1993; Klar and Randolph, 2008).

Quantitatively, the average N_p value resulting from the rotational flow mechanism was only about 50% of that due to the full flow mechanism (see the API reference line in Fig. 18(b)). This is because smaller areas of soil had mobilised its strength in the former mechanism than the latter, as illustrated in earlier part of this section.

It is expected that the N_p value would increase with the distance from the rotation point, which is located in the mid-depth of zone III. The non-zero N_p at the rotation point implies a translational movement of the semi-rigid pile at that point.

Compared to the measured and computed results, the API (2007) code underestimated the N_p values for the pile embedded in the full-flow region (i.e., zone II). This is possibly because the N_p values in the API (2007) was deduced from two-way cyclic loading tests, which should have resulted in more reduction in s_u (and hence N_p) than that in the one-way cyclic loading tests in this study. In the rotational soil flow region (i.e., zone III), both measured and computed N_p values were overestimated by the code, which assumes a full-flow mechanism without considering the altered mechanism in relation to the semi-rigid pile.

For the rigid pile, as shown in Fig. 18(c), it was expected that the computed N_p value along the upper half of the pile would increase with depth (i.e., zone I, where a wedge mechanism dominated). Along the lower half of the pile (i.e., zone II, corresponding to a rotational soil flow mechanism), the computed N_p profile exhibited a bilinear distribution, i.e., increasing with the distance from the rotation point, which was at the mid-depth of zone II. The distribution of N_p suggested by the code, however, shows a single trend of increase along the entire pile length. This is because

the code simply assumes a wedge mechanism within a depth of $4D$, without consideration of the altered wedge depth for a large diameter pile (about $2D$ for the rigid pile shown in Fig. 18(c)).

Summary and conclusions

This study has investigated the cyclic response of and the mechanisms of soil flow around a semi-rigid pile and a jet-grouting-reinforced pile, through monotonic and cyclic centrifuge model tests supplemented by finite element analyses using an advanced hypoplastic clay model. Based on the physical and numerical investigation, the following conclusions can be drawn:

1. The cyclic lateral head displacements of the semi-rigid pile showed a shakedown response when subjected to the first two episodes of one-way cycling (cyclic magnitudes=15-30% and 15-45% F_u , where F_u is the ultimate lateral pile capacity). On the other hand, a ratcheting response resulted when the cyclic magnitude increased to 15-60% F_u in the third episode of cycling. At the end of the third loading episode, the irrecoverable pile head displacement accounted for about 90% of the total displacement. This implies that the lateral pile displacement was mainly induced by cumulative plastic strains in the soil surrounding the cyclically loaded pile.
2. Positive excess pore water pressure was generated in the slightly over-consolidated clay during each episode of cycling as anticipated. The accumulation of pore water pressure with cycling showed a similar trend to that of

the cumulative lateral pile head displacement, i.e., a shakedown response during the first two loading episodes and a ratcheting response during the third episode of cycling.

3. In each episode of cycling, the semi-rigid pile behaved as if it were a flexible pile (flexural deformation dominated) during the first few cycles. In contrast, it behaved as a rigid pile (rotational movement prevailed) when the number of loading cycles increased. The altering deflection modes of the semi-rigid pile during cycling was likely attributed to the degraded soil stiffness as a result of cumulative positive pore pressure and plastic shear strain, causing an increased relative pile-soil stiffness. These trends should be further confirmed by performing one more test on semi-rigid pile with a relative soil-pile stiffness $\frac{E_p I_p}{E_s l_L^4}$ exceeding 0.0067 (as adopted in this study) but smaller than that of a fully rigid pile.
4. The soil flows around the laterally loaded semi-rigid pile were comprised of three distinctive mechanisms, i.e., a wedge-type mechanism near the surface, a full-flow mechanism (developed within the transverse section across the pile) near the middle of the pile and a rotational soil flow mechanism (developed in the vertical symmetrical plane of the pile) along the lower half of the pile. The numerical parametric study revealed that the soil flow mechanisms around the semi-rigid pile exhibited an intermediate behavior combining the mechanisms of a flexible pile (a wedge-type mechanism near the surface and a full-flow mechanism at greater depth) and a rigid pile (a wedge-type mechanism near the surface and a rotational soil flow mechanism at greater depth). The combined soil flow

mechanisms are compatible with the altering deflection mode (from a flexible to a rigid pile during cycling) of the semi-rigid pile.

5. The API (2007) code, which assumes a full-flow mechanism at depth with a constant bearing capacity factor (i.e., 6.5), overestimated the resistance factor (with an average of 4.5) for the rotational soil flow at the lower half of the semi-rigid pile. Consequently, the use of the cyclic p - y curves of the code underestimated the cyclic bending moment and the lateral pile head displacement by 10 and 69%, respectively. In other words, the API code may not yield conservative estimates after all, as it was developed based on experiments of flexible piles for predicting the bending moment and lateral displacement of a semi-rigid pile.
6. After applying jet-grouting (with an outer diameter and depth of 1.68 and 6 m, respectively) around the semi-rigid pile at a shallow depth, the pile behaved as a rigid pile (rotational movement dominated) throughout the entire cycling process. The soil displacements around the cyclically loaded pile mainly occurred within a wedge extending from the bottom of the grouting to the ground surface, meaning that the lateral loading can be sufficiently resisted by the soil around the grouted zone near the surface. Consequently, the presence of the jet-grouting reduced the cumulative cyclic pore pressure in the soil and therefore the lateral pile head displacement by 75 and 80%, as compared to those of the semi-rigid pile.

Although fairly large rotations of piles were considered in this study for revealing failure mechanisms of the soil around the pile, the tolerable rotation of piles

supporting deformation-sensitive offshore structures (such as wind turbine) is typically less than 0.5° (including installation tolerance of 0.25°). It is of practical relevance and significance to perform further tests on semi-rigid piles without jet-grouting under more reasonable cyclic amplitudes.

Acknowledgements

The authors gratefully acknowledge the financial support provided by the Distinguished Young Scholars of China (Grant No. 51325901) and International Science & Technology Cooperation Program of China (2015DFE72830).

References

- Al-Tabbaa, A. 1987. Permeability and stress-strain response of speswhite kaolin. Ph.D. thesis, University of Cambridge.
- American Petroleum Institute (API) 2007. Recommended Practice for Planning, Designing and Constructing Fixed Offshore Platforms-Working Stress Design. API
- Bolton, M.D., and Stewart, D.I. 1994. The effect on propped diaphragm walls of rising groundwater in stiff clay. *Géotechnique*, 44, 111-111.
- Briaud, J.L. 1984. Panel discussion, laterally loaded deep foundation (STP 835), ASTM, Philadelphia, 239–243.
- Budhu, M., and Davies, T. 1988. Analysis of Laterally Loaded Piles in Soft Clays. *J. Geotech. Engrg.*, 114(1), 21–39.
- Chen, L., and Poulos, H.G. 1993. Analysis of pile-soil interaction under lateral loading using infinite and finite elements. *Computers and Geotechnics*, 15(4), 189-220.
- Dobry, R., Vicente, E., O'Rourke, M., and Roesset, M. 1982. Horizontal stiffness and damping of single piles. *Journal of Geotechnical and Geoenvironmental Engineering*, 108(GT3).
- Gao, F.P., Li, J.H., Qi, W.G., Hu, C. 2015. On the instability of offshore foundations: theory and mechanism. *Science China -- Physics, Mechanics & Astronomy*, 2015, 58 (12): 124701.
- Georgiadis, M., Anagnostopoulos, C., and Saflekou, S. 1992. Cyclic lateral loading of piles in soft clay. *Geotechnical engineering*, 23(1).
- Gourvenec, S., Acosta-Martinez, H.E., and Randolph, M.F. 2009. Experimental study of uplift resistance of shallow skirted foundations in clay under transient

- and sustained concentric loading. *Géotechnique*, 59(6), 525-537.
- Haiderali, A.E., Nakashima, M., and Madabhushi, S.P.G. 2015. Cyclic lateral loading of monopiles for offshore wind turbines. 3rd International Symposium on Frontiers in Offshore Geotechnics (ISFOG 2015), At Oslo, Norway.
- Hamilton, J.M., Phillips, R., Dunnivant, T.W., and Murff, J.D. 1991. Centrifuge study of laterally loaded pile behavior in clay. In Proc., Int. Conf. Centrifuge (Vol. 91, pp. 285-292).
- He, B. 2016. Lateral behaviour of single pile and composite pile in soft clay. Ph.D. thesis, Zhejiang University, CN.
- He, B., Wang, L. Z., Hong, Y. 2016. Field testing of one-way and two-way cyclic lateral responses of single and jet-grouting reinforced piles in soft clay. *Acta Geotechnica*, accepted.
- Hong, Y., Ng, C. W. W. and Wang, L. Z. 2015. Initiation and failure mechanism of base instability of excavations in clay triggered by hydraulic uplift. *Canadian Geotechnical Journal*. 52(5), 599-608.
- Hu C., Liu H.X., Huang W 2012. Anisotropic bounding-surface plasticity model for the cyclic shakedown and degradation of saturated clay. *Computers and Geotechnics*, 44, 34-47.
- Inagaki, M., Abe, T., Yamamoto, M., Nozu, M., Yanagawa, Y. & Li, L. 2002. Behaviour of cement deep mixing columns under road embankment. Proceedings of the international conference on physical modelling in geotechnics, St John's, Newfoundland, pp. 967–972.
- Jeanjean, P. 2009. Re-assessment of P-Y curves for soft clays from centrifuge testing and finite element modeling. In Offshore Technology Conference. Offshore Technology Conference.
- Khemakhem, M., Chenaf, N., Garnier, J., Favraud, C., and Gaudicheau, P. 2012. Development of Degradation Laws For Describing the Cyclic Lateral Response of Piles In Clay. Offshore Site Investigation and Geotechnics: Integrated Technologies-Present and Future. Society of Underwater Technology.
- Khemakhem, M., Chenaf, N., Garnier, J., Favraud, C., and Gaudicheau, P. 2012. Development of Degradation Laws For Describing the Cyclic Lateral Response of Piles In Clay [J]. Offshore Site Investigation and Geotechnics: Integrated Technologies-Present and Future. Society of Underwater Technology.
- Khemakhem, M., Chenaf, N., Garnier, J., Rault, G., Thorel, L., and Dano, C. 2010. Static and cyclic lateral pile behavior in clay. In 7th international Conference on Physical Modelling in Geotechnics (pp.953).
- Kitazume, M., Okano, K. & Miyajima, S. 2001. Centrifuge model tests on failure envelope of column type DMM improved ground (Discussion). *Soils and Foundations*, 41(4), 108.
- Klar, A., and Randolph, M.F. 2008. Upper-bound and load-displacement solutions for laterally loaded piles in clays based on energy minimisation. *Géotechnique*,

- 58(10), 815.
- Kulhawy, F.H., and Chen, Y.J. 1995. A thirty-year perspective of Broms' lateral loading models, as applied to drilled shafts. *Bengt. B. Broms Symp. Geotech. Eng., NTU-PWD Geotechnical Research Centre, Singapore*, 225–240.
- Loganathan, N., Poulos, H.G., and Stewart, D.P. 2000. Centrifuge model testing of tunnelling-induced ground and pile deformations. *Geotechnique*, 50(3), 283-294.
- Mašín, D. 2014. Clay hypoplasticity model including stiffness anisotropy. *Géotechnique* 64(3):232–238
- Mašín, D. 2005. A hypoplastic constitutive model for clays. *International Journal for Numerical and Analytical Methods in Geomechanics*, 29(4): 311-336.
- Mašín, D., Herle, I. 2005. State boundary surface of a hypoplastic model for clays. *Computers and Geotechnics*, 32(6): 400-410.
- Matlock, H. 1970. Correlations for design of laterally loaded piles in clay. *Proceedings of the Offshore Technology Conference, Houston, Paper OTC1204*, pp. 577–588.
- Matlock, H. 1970. Correlations for design of laterally loaded piles in clay. *Proceedings of the Offshore Technology Conference, Houston, Paper OTC1204*, pp. 577–588.
- Matsuoka, H., and Nakai, T. 1974. Stress-deformation and strength characteristics of soil under three different principal stresses. *Proceedings of the Japanese Society of Civil Engineers ; 232:59–70*.
- Mayne, P.W., Kulhawy, F.H., and Trautmann, C.H. 1995. Laboratory modeling of laterally-loaded drilled shafts in clay. *Journal of geotechnical engineering*, 121(12), 827-835.
- Mayne, P.W., Kulhawy, F.H., and Trautmann, C.H. 1995. Laboratory modeling of laterally-loaded drilled shafts in clay. *Journal of geotechnical engineering*, 121(12), 827-835.
- Mayne, P.W. and Fred, H.K. 1982. Ko-OCR relationships in soil. *Journal of the Geotechnical Engineering Division*, 108 (6), 851-872.
- Murali, M., Grajales, F., Beemer, R.D., et al. 2015. Centrifuge and Numerical Modeling of Monopiles for Offshore Wind Towers Installed in Clay. *ASME 2015 34th International Conference on Ocean, Offshore and Arctic Engineering. American Society of Mechanical Engineers*.
- Murff, J.D., and Hamilton, J.M. 1993. P-ultimate for undrained analysis of laterally loaded piles. *Journal of Geotechnical Engineering*, 119(1), 91-107.
- Ng, C.W.W., Zhang, L.M., and Nip, C.N. 2001. Response of laterally loaded large-diameter bored pile groups. *Journal of Geotechnical and Geoenvironmental Engineering* 127(8): 642–657.
- Ng W.W., Poulos H.G., Chan S.H., Lam S.Y., Chan C.Y. 2008. Effects of tip location and shielding on piles in consolidating ground. *Journal of Geotechnical and Geoenvironmental Engineering*, 134(9): 1245-1260.
- Niemunis, A., and Herle, I. 1997. Hypoplastic model for cohesionless soils with

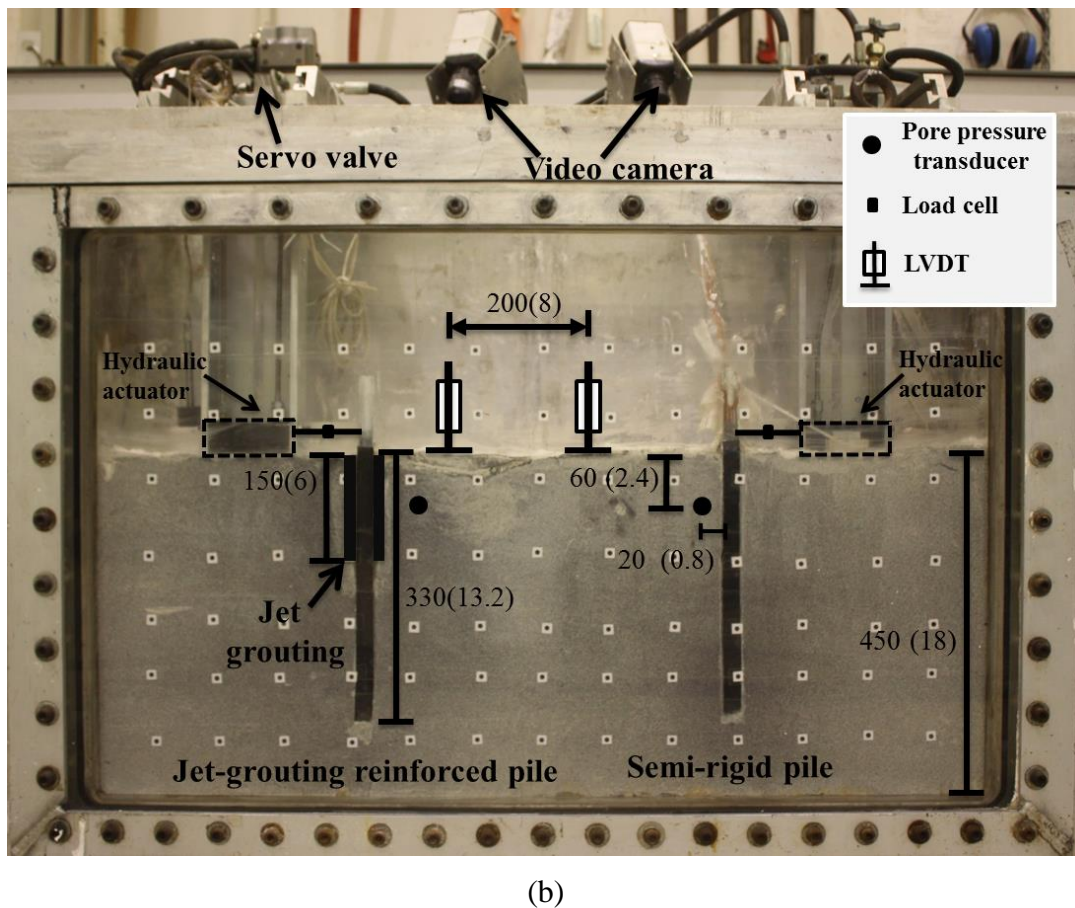
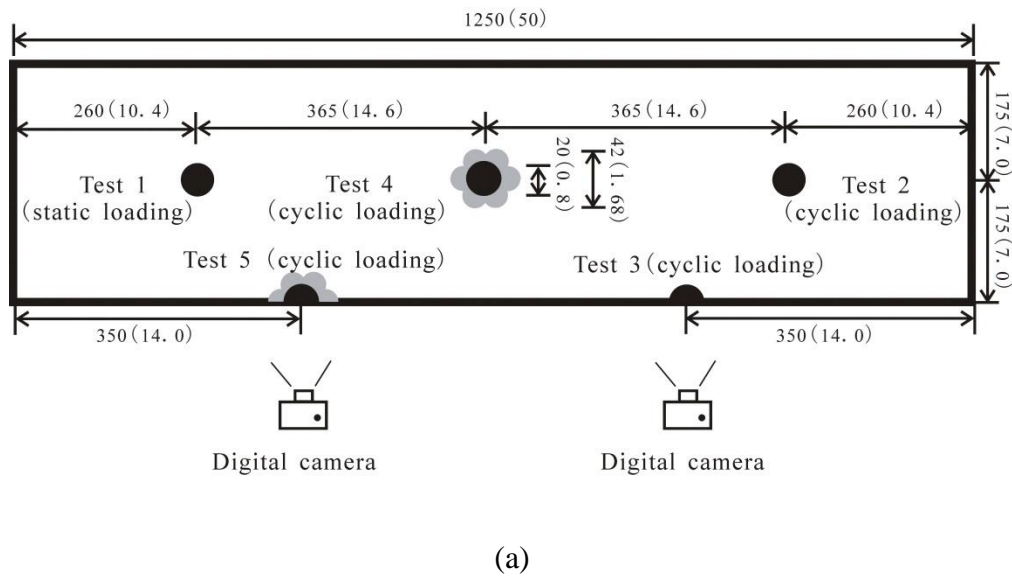
- elastic strain range. *Mech. Cohesive-Frict. Mater.*, 2, 279-299.
- Nishida, K., Koga, Y. & Miura, N. 1996. Energy consideration of the dry jet mixing methods. *Proc. 2nd Int. Conf. on Ground Improvement Geosystems*, Tokyo 1, 643–648.
- Poulos, H.G., and Hull, T.S. 1989. The role of analytical geomechanics in foundation engineering. *Foundation Engineering@ Current Principles and Practices*. ASCE: 1578-1606.
- Poulos, H.G., and Davis, E.H. 1980. *Pile foundation analysis and design*. Wiley, New York.
- Randolph, M.F., and Wroth, C.P. 1981. Application of the failure state in undrained simple shear to the shaft capacity of driven piles. *Geotechnique*, 31(1): 143-157.
- Reese, L.C., and Van Impe, W.F. 2001. *Single piles and pile groups under lateral loading*. Balkema, Rotterdam, The Netherlands.
- Stevens, J.B., and Audibert, J.M.E. 1979. Re-examination of py curve formulations. In *Offshore Technology Conference*. Offshore Technology Conference.
- Stewart, D.P., and Randolph, M.F. 1991. A new site investigation tool for the centrifuge. In *Proc. Int. Conf. Centrifuge* (Vol. 91, pp. 531-538).
- Systèmes, D. 2007. *Abaqus analysis user's manual*. Simulia Corp. Providence, RI, USA.
- Tan, T.S., Inoue, T., and Lee, S.L. 1991. Hyperbolic method for consolidation analysis. *Journal of Geotechnical Engineering*, 117(11), 1723-1737.
- Terzaghi, K. 1943. *Theoretical Soil Mechanics*. John Wiley and Sons, New York.
- Wang, L. Z., Chen, K. X., Hong, Y. and Ng, C. W. W. 2014. Effect of consolidation on responses of a single pile subjected to lateral soil movement. *Canadian Geotechnical Journal* 52(6), 769-782.
- Wang, L.Z., He, B., Hong, Y., Guo, Z., and Li, L.L. 2015. Field tests of the lateral monotonic and cyclic performance of jet-grouting reinforced cast-in-place piles. *Journal of Geotechnical and Geoenvironmental Engineering* 141(5).
- Wroth, C. and Houlsby, G. 1985. Soil mechanics–property characterisation, and analysis procedures. *Proceedings of the 11th international conference on soil mechanics and foundation engineering*, San Francisco, vol. 1, pp. 1–55. Rotterdam, the Netherlands: Balkema.
- Zhang, C., White, D., and Randolph, M. 2011. Centrifuge Modeling of the Cyclic Lateral Response of a Rigid Pile in Soft Clay. *Canadian Geotechnical Journal* 137(7), 717-729.

Caption of Figures

- Fig. 1. Centrifuge model package: (a) plan view; (b) elevation view
- Fig. 2. (a) Servo-controlled cyclic loading system; (b) connection between the half-model pile and the cyclic loading system
- Fig. 3. Distribution of (a) undrained shear strength and (b) over-consolidation ratio with depth
- Fig. 4. Measured monotonic load-displacement relationship of the semi-rigid pile
- Fig. 5. Measured cyclic load-displacement relationship at the head of the semi-rigid pile
- Fig. 6. (a) Measured lateral pile head displacement of the semi-rigid pile; (b) measured lateral pile head displacement of jet-grouting reinforced pile; (c) measured and curve-fitted relationship between $\delta_{h-n}/\delta_{h-1}$ and N for the semi-rigid pile and (d) measured and curve-fitted relationship between $\delta_{h-n}/\delta_{h-1}$ and N for the jet-grouting reinforced pile
- Fig. 7. Measured cyclic pore water pressure in front of (a) the semi-rigid pile and (b) the jet-grouting reinforced pile
- Fig. 8. Measured lateral deformation of the semi-rigid pile during: (a) the first episode of cycling; (b) the second episode of cycling; and (c) the third episode of cycling
- Fig. 9. Measured soil flow mechanism around the semi-rigid pile during the third episode of cycling: (a) 1st loading cycle; (b) 50th loading cycle; (c) 100th loading cycle.
- Fig. 10. Measured soil flow mechanism around the jet-grouting reinforced pile during the third episode of cycling: (a) 1st loading cycle; (b) 50th loading cycle; (c) 100th loading cycle
- Fig. 11. Measured bending moment profiles of the semi-rigid pile and the jet-grouting reinforced pile due to the 1st, 50th and 100th lateral loading during the third episode of cycling (cyclic magnitude = 15-60% F_u)
- Fig. 12. Deduced cyclic p-y relationships at typical depths: (a) 4D, (b) 7D

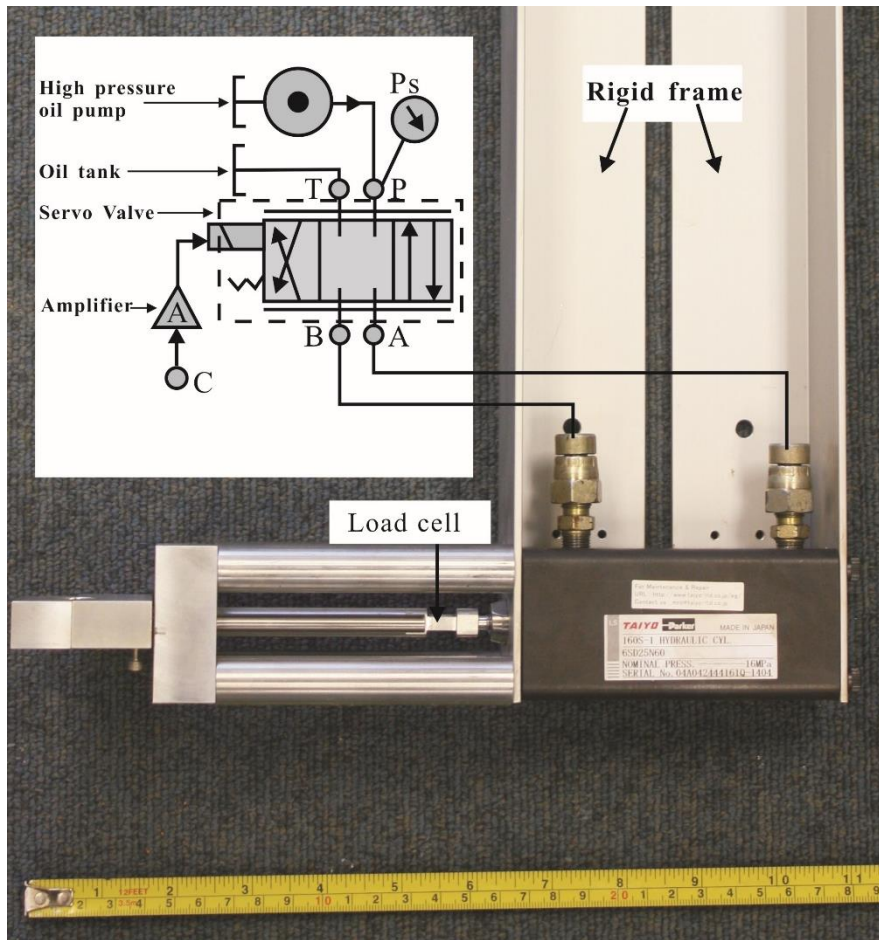
and (c) $10D$

- Fig. 13. Comparison of the measured and calculated (based on API, 2007): (a) pile displacement and (b) bending moment
- Fig. 14. Three-dimensional finite element mesh and boundary conditions
- Fig. 15. Comparison of the measured and computed stress-strain relationship of a soil element subjected to cyclic triaxial shearing
- Fig. 16. Comparison of the measured and computed cumulative lateral pile head displacement
- Fig. 17. Computed soil flow mechanisms around cyclically loaded piles with various diameters: (a) semi-rigid pile flexible pile ($D=0.8\text{m}$); (b) flexible pile ($D=0.3\text{m}$); and (c) rigid pile ($D=4\text{m}$)
- Fig. 18. Computed lateral bearing capacity factors along pile depth: (a) flexible pile ($D=0.3\text{m}$); (b) semi-rigid pile ($D=0.8\text{m}$); and (c) rigid pile ($D=4\text{m}$)

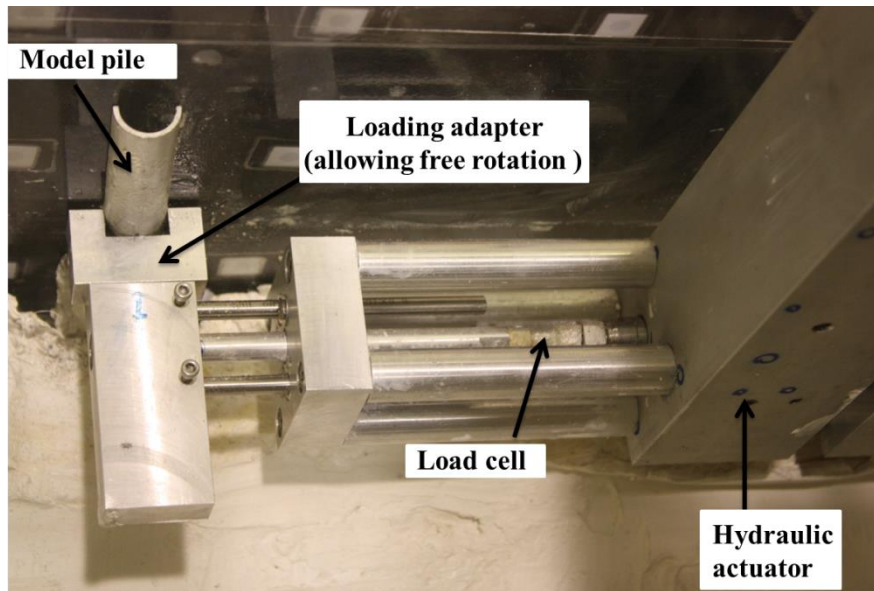


Note: All dimensions are in millimeters except for numbers in parentheses, which denote prototype scale (unit: m).

Fig. 1. Centrifuge model package: (a) plan view; (b) elevation view



(a)



(b)

Fig. 2. (a) Servo-controlled cyclic loading system; (b) connection between the half-model pile and the cyclic loading system

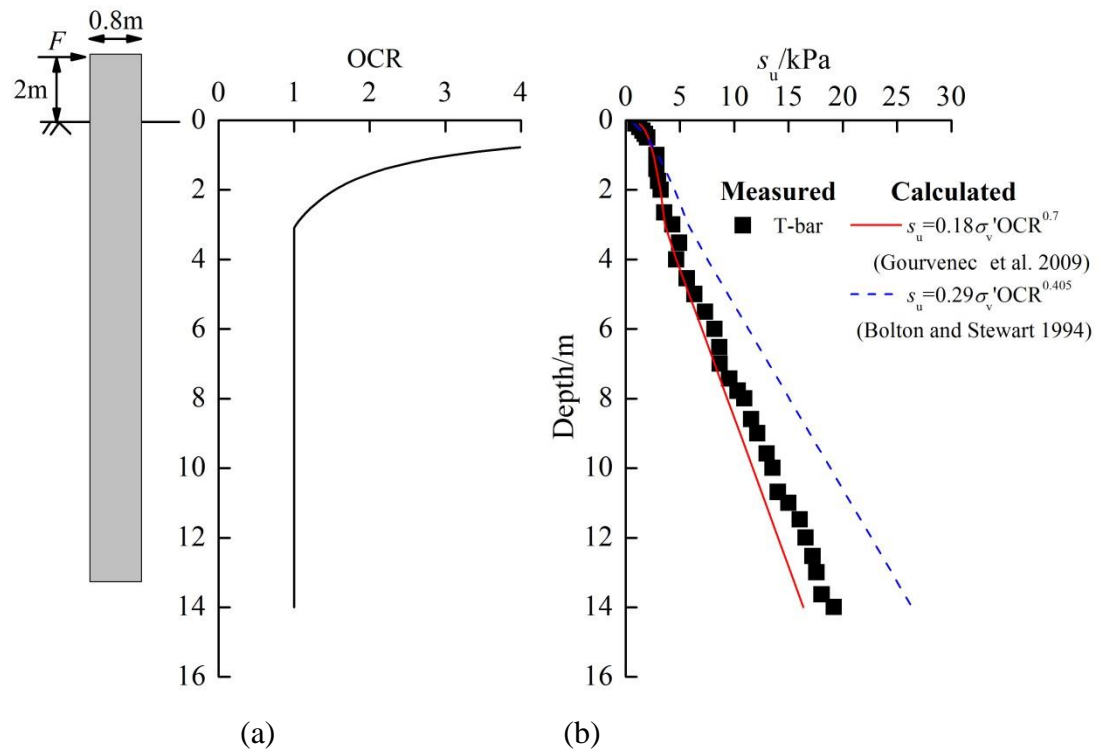


Fig. 3. Distribution of (a) undrained shear strength and (b) over-consolidation ratio with depth

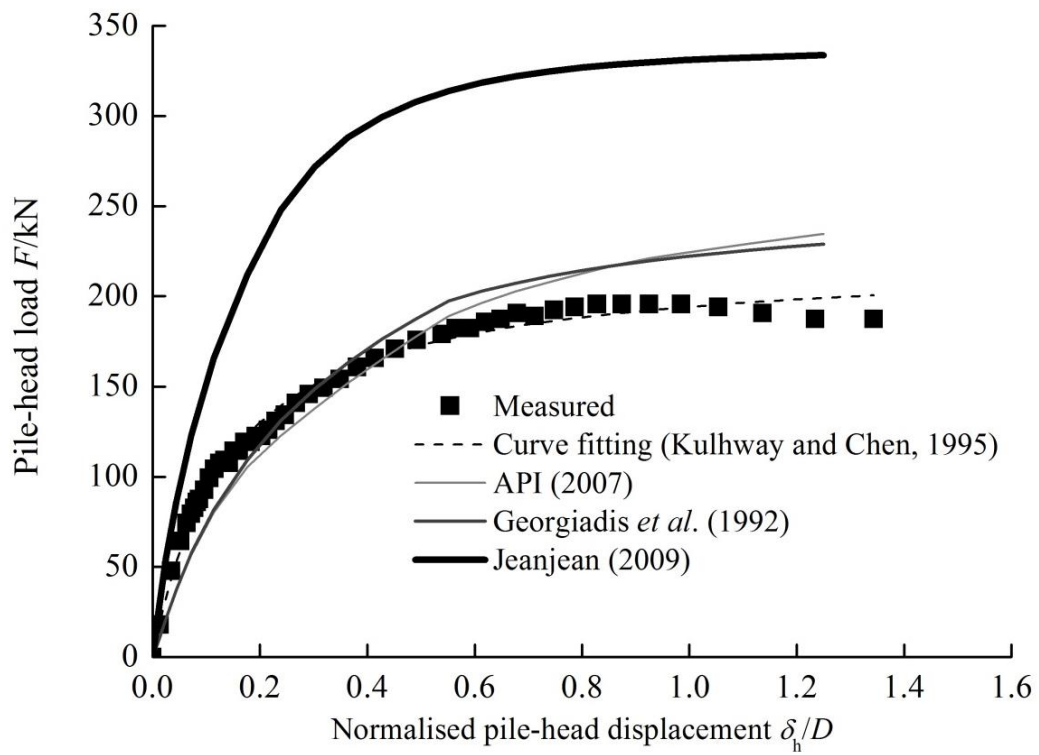


Fig. 4. Measured monotonic load-displacement relationship at the head of of the semi-rigid pile

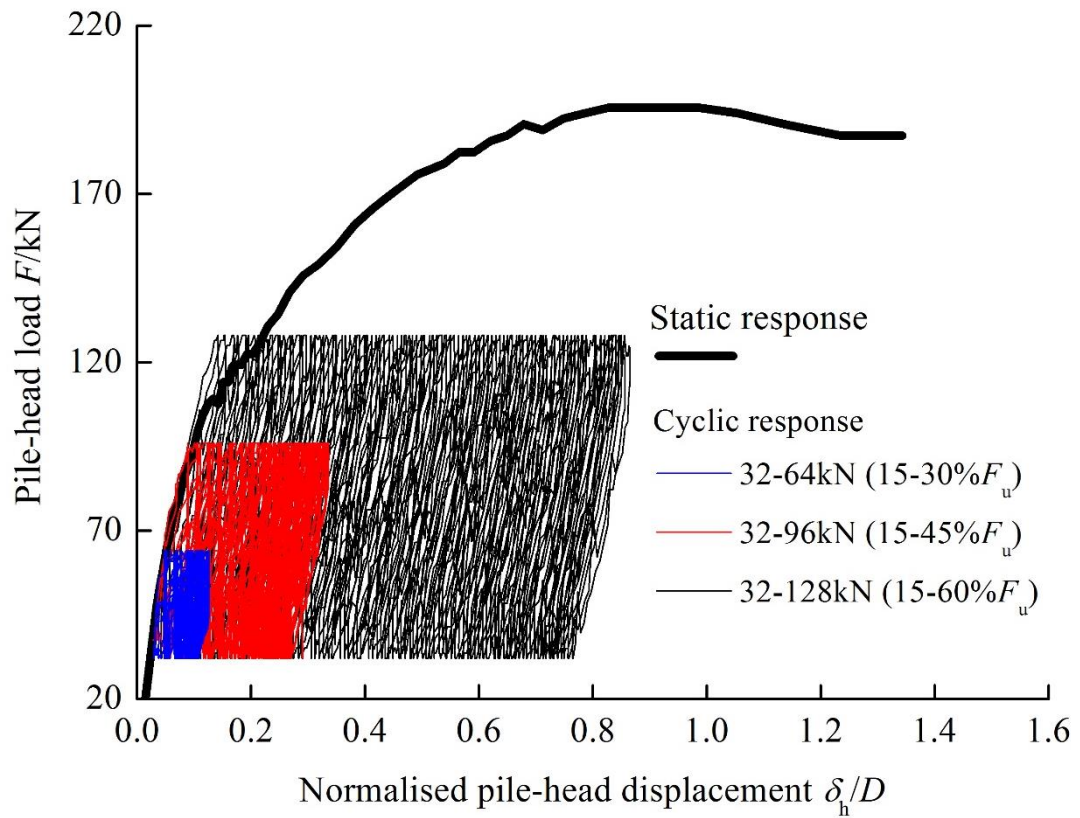


Fig. 5. Measured cyclic load-displacement relationship at the head of the semi-rigid pile

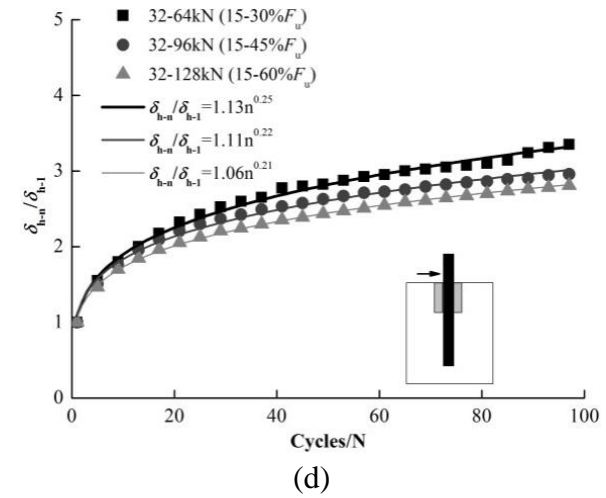
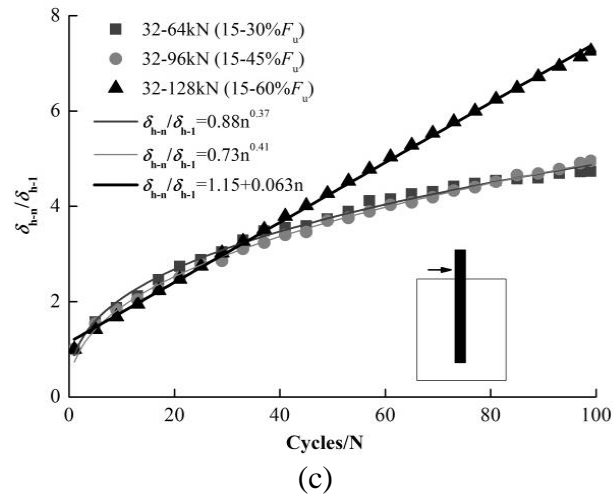
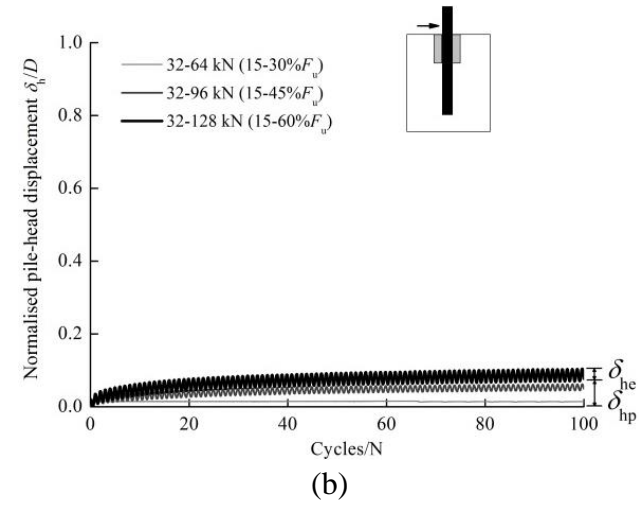
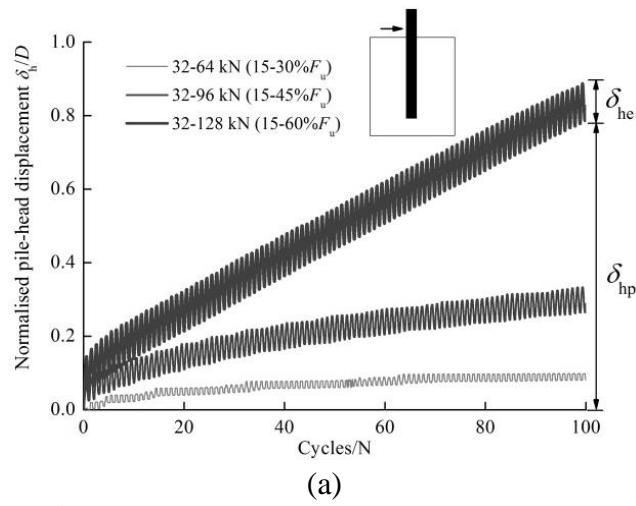
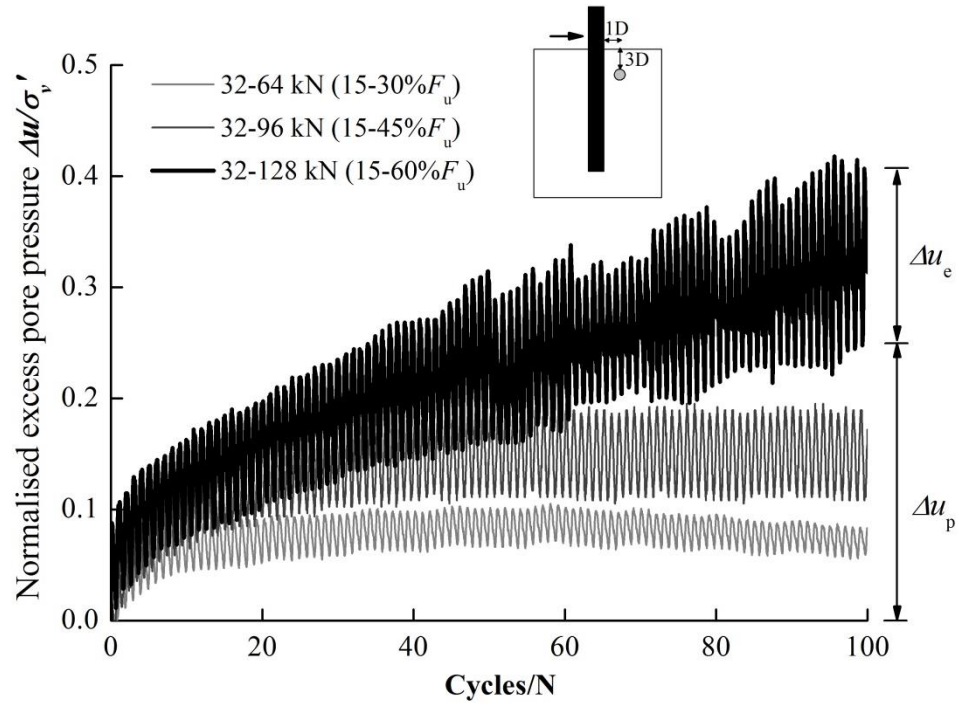
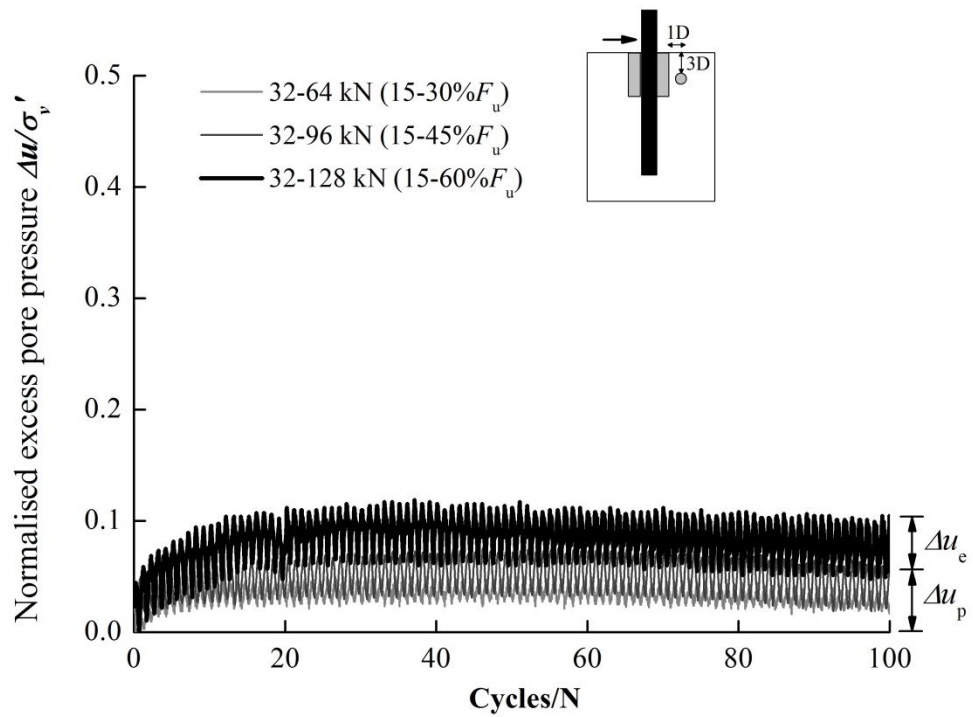


Fig. 6. (a) Measured lateral pile head displacement of the semi-rigid pile; (b) measured lateral pile head displacement of jet-grouting-reinforced pile; (c) measured and curve-fitted relationship between $\delta_{h-n}/\delta_{h-1}$ and N for the semi-rigid pile; and (d) measured and curve-fitted relationship between $\delta_{h-n}/\delta_{h-1}$ and N for the jet-grouting-reinforced pile.

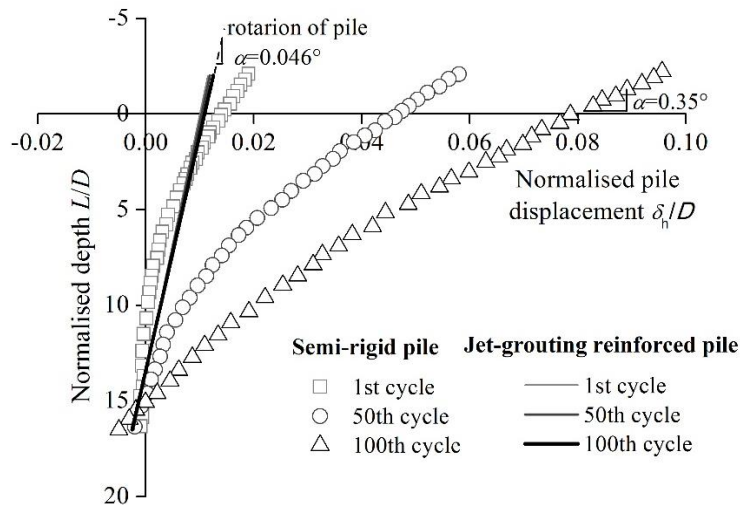


(a)

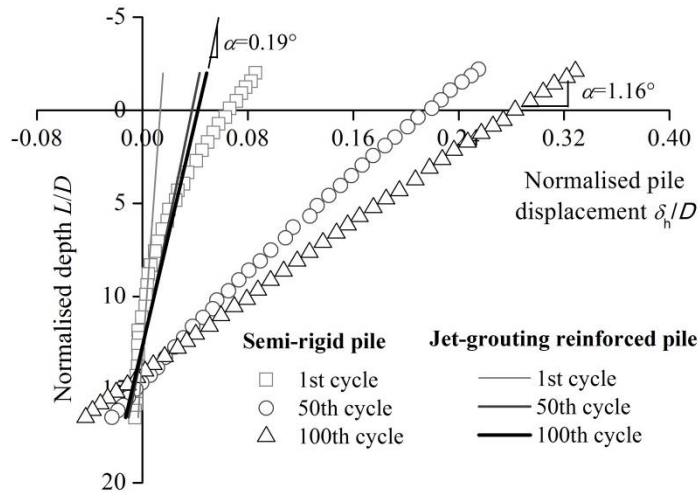


(b)

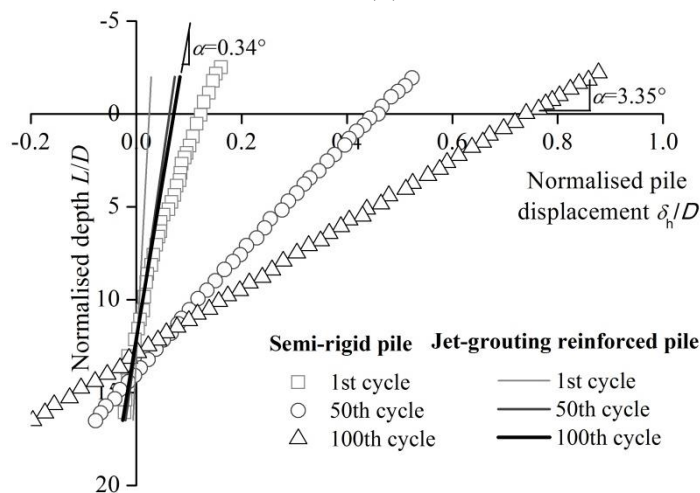
Fig. 7. Measured cyclic pore water pressure in front of (a) the semi-rigid pile and (b) the jet-grouting-reinforced pile



(a)



(b)



(c)

Fig. 8. Measured lateral deformation of the semi-rigid pile and jet-grouting-reinforced pile during: (a) the first episode of cycling; (b) the second episode of cycling; and (c) the third episode of cycling.

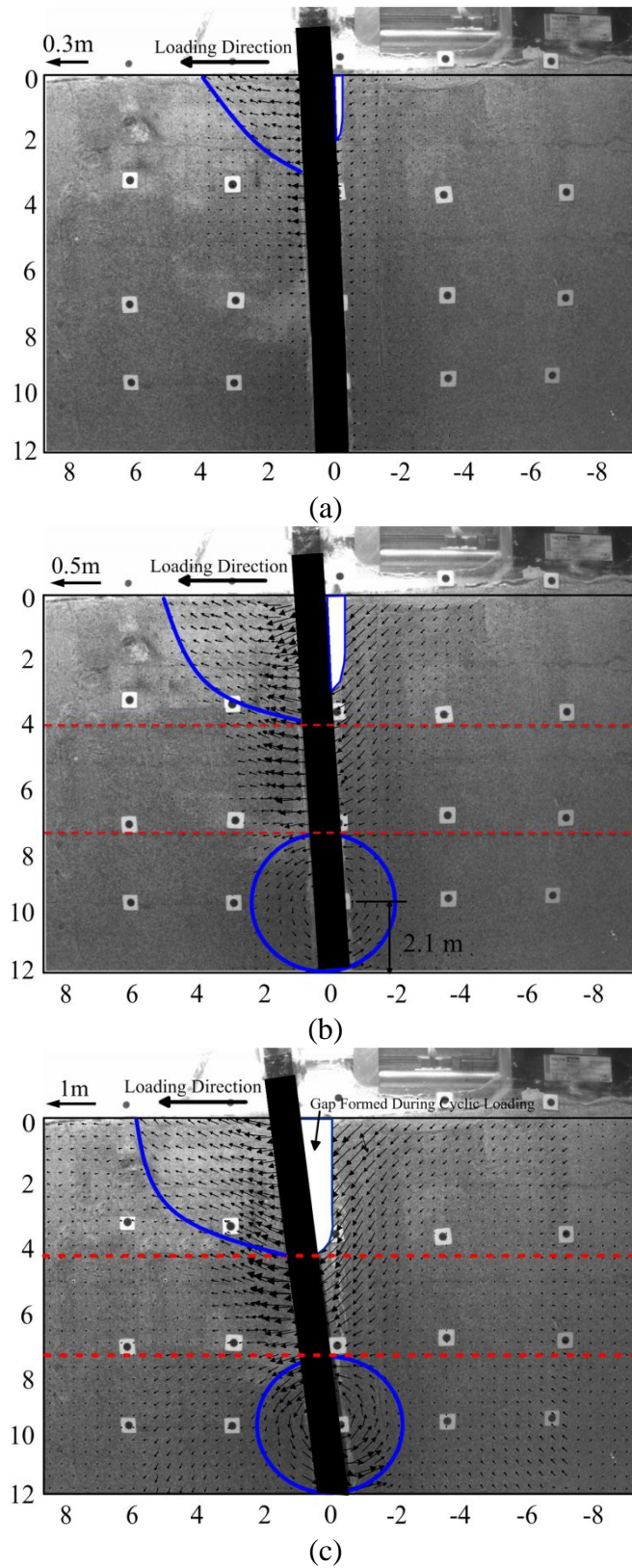
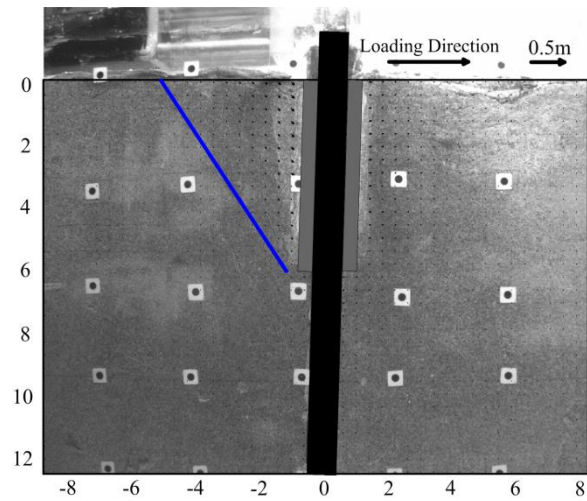
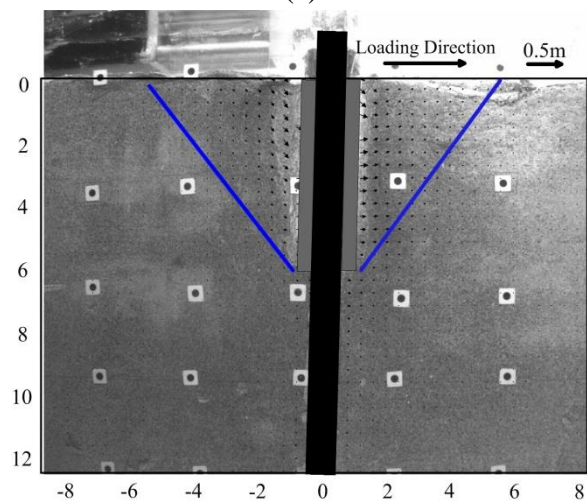


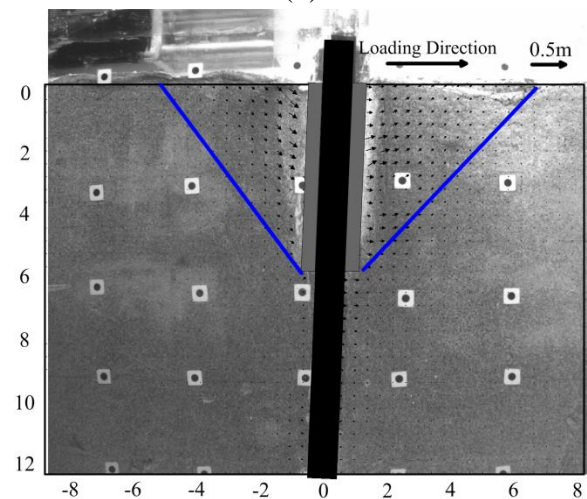
Fig. 9. Measured soil flow mechanism around the semi-rigid pile during the third episode of cycling: (a) 1st loading cycle; (b) 50th loading cycle; and (c) 100th loading cycle.



(a)



(b)



(c)

Fig. 10. Measured soil flow mechanism around the jet-grouting-reinforced pile during the third episode of cycling: (a) 1st loading cycle; (b) 50th loading cycle; and (c) 100th loading cycle.

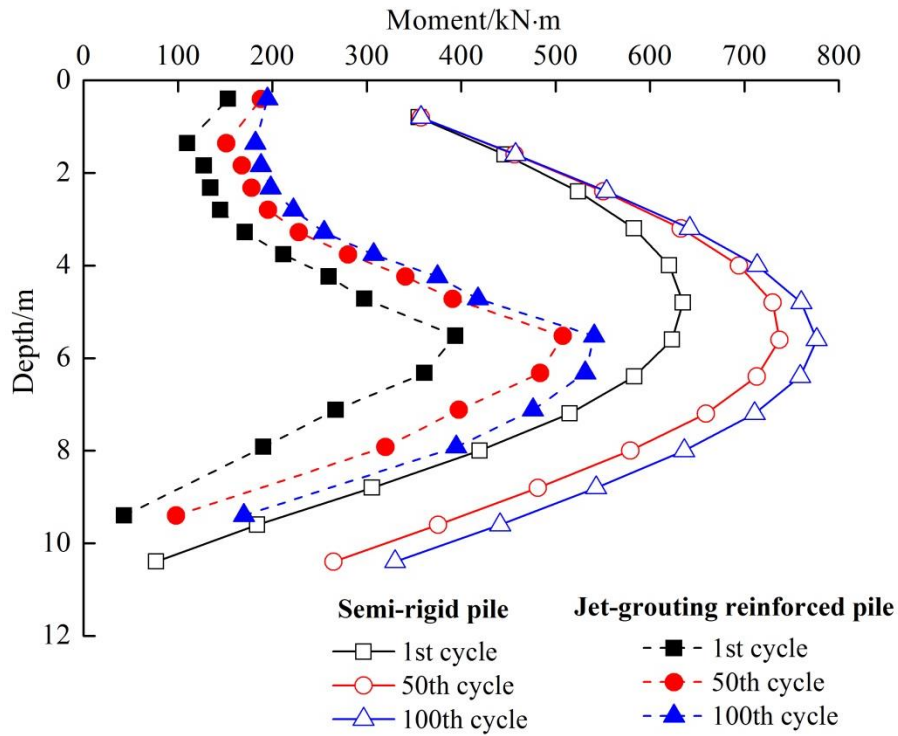
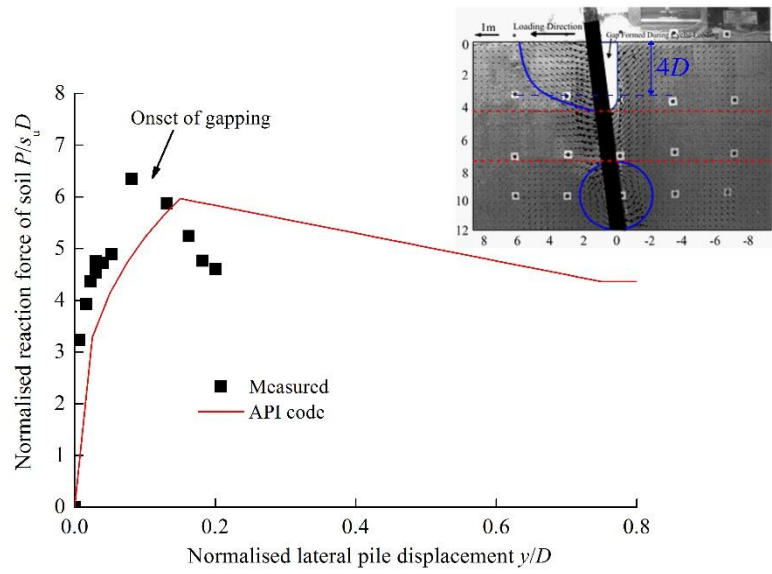
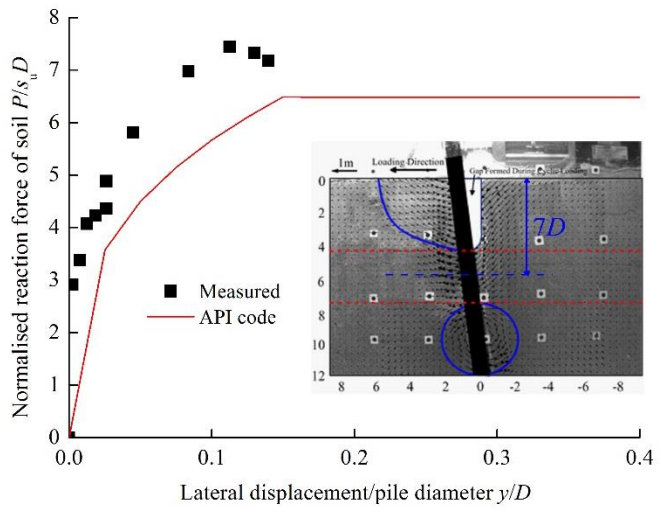


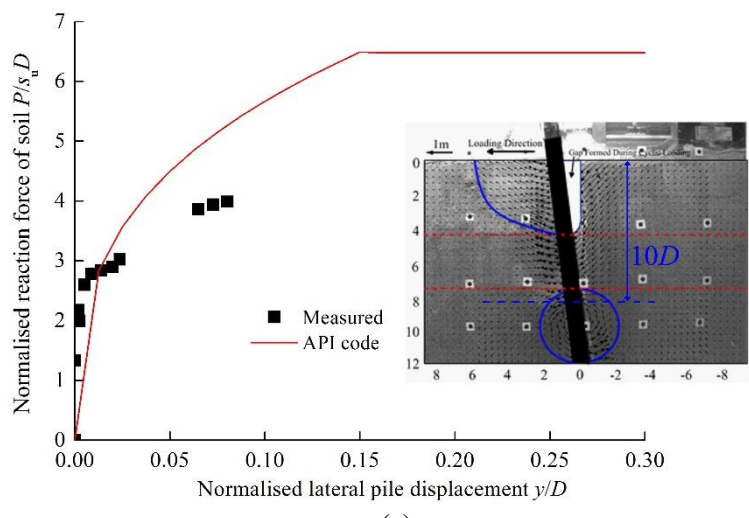
Fig. 11. Bending moment profiles of the semi-rigid pile and the jet-grouting-reinforced pile due to the 1st, 50th and 100th lateral loading during the third episode of cycling (cyclic magnitude = 15-60% F_u)



(a)



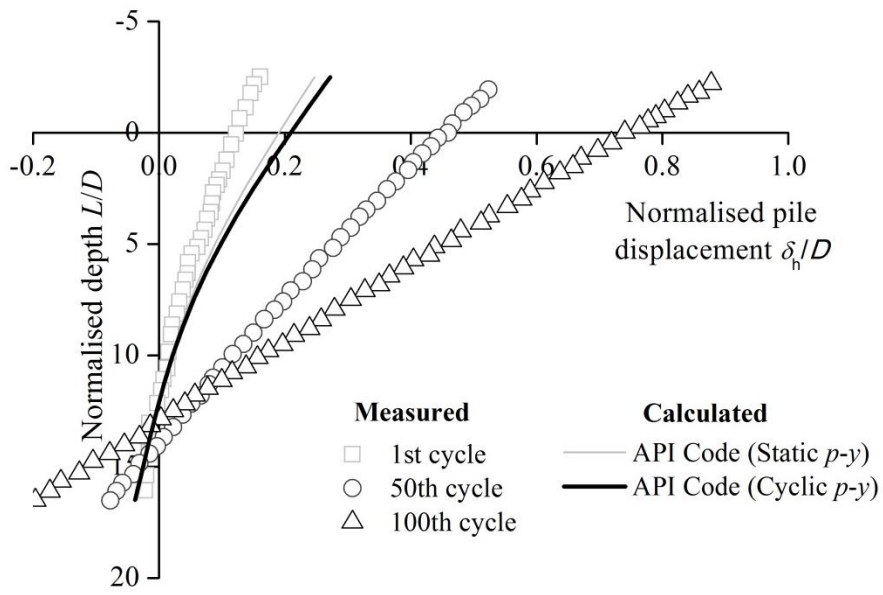
(b)



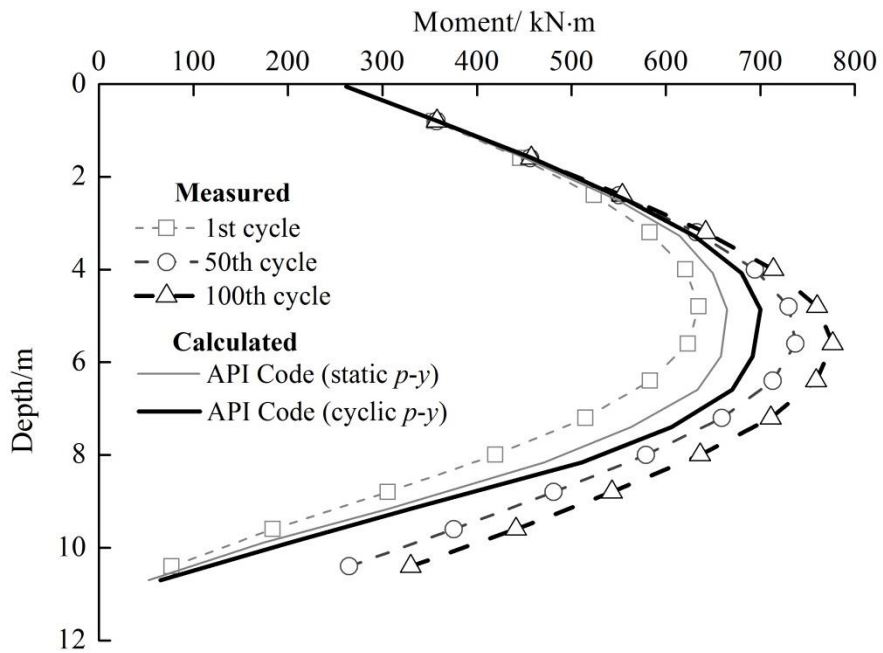
(c)

Fig. 12. Deduced cyclic p-y relationships at typical depths: (a) 4D, (b) 7D and (c)

10D

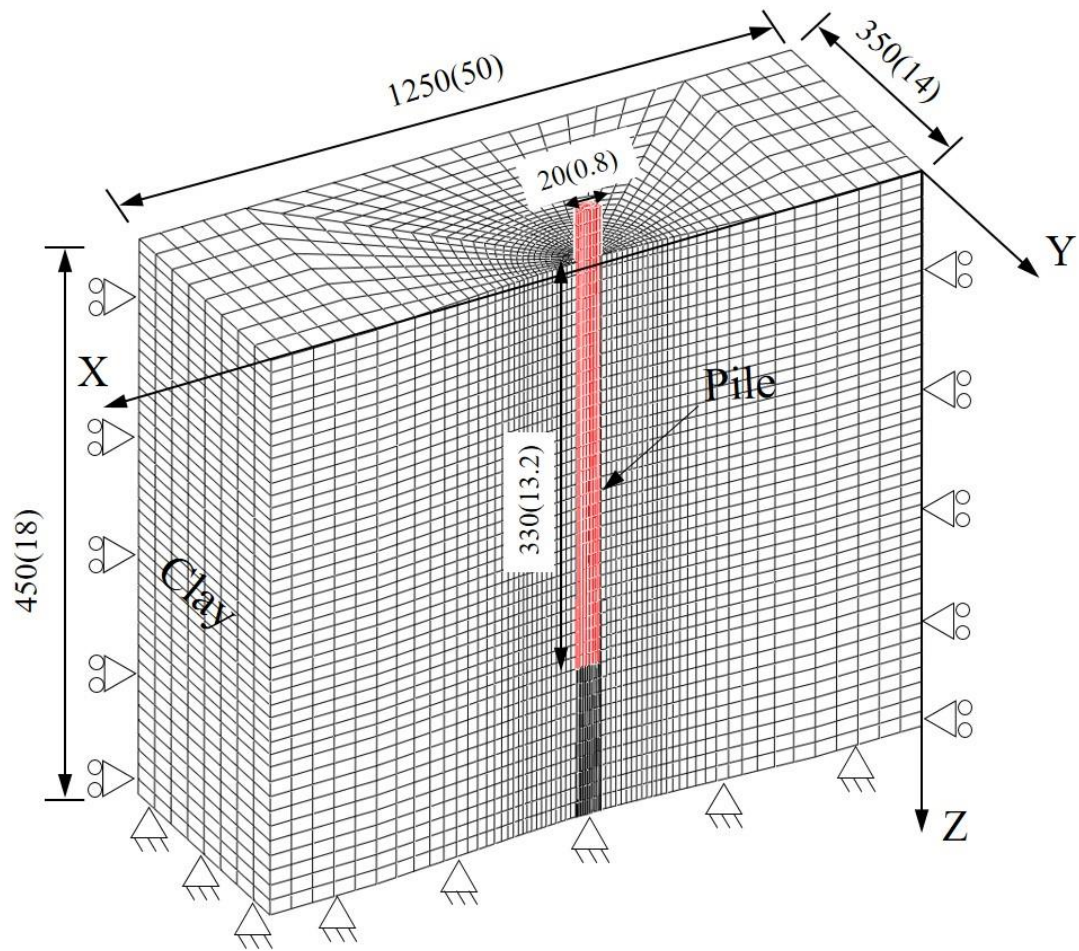


(a)



(b)

Fig. 13. Comparison of the measured and calculated (based on API, 2007) (a) pile displacement and (b) bending moment.



Note: All dimensions are in millimeters except for numbers in parentheses, which denote prototype scale (unit: m).

Fig. 14. Three-dimensional finite element mesh and boundary conditions

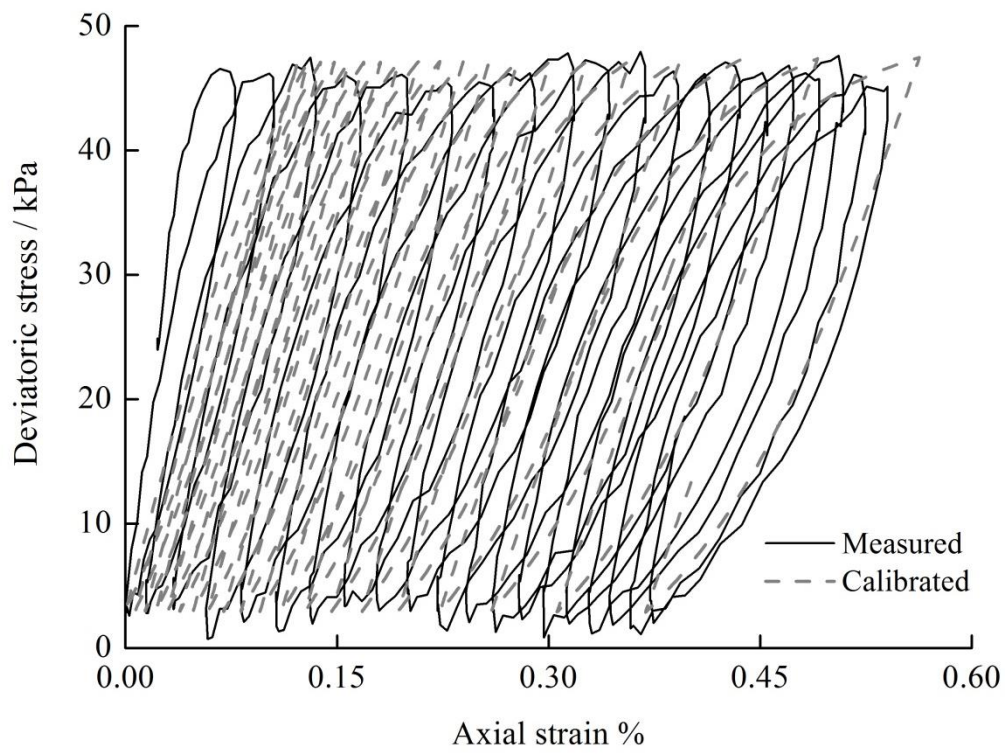


Fig. 15. Comparison of the measured and computed stress-strain relationship of a soil element subjected to cyclic triaxial shearing

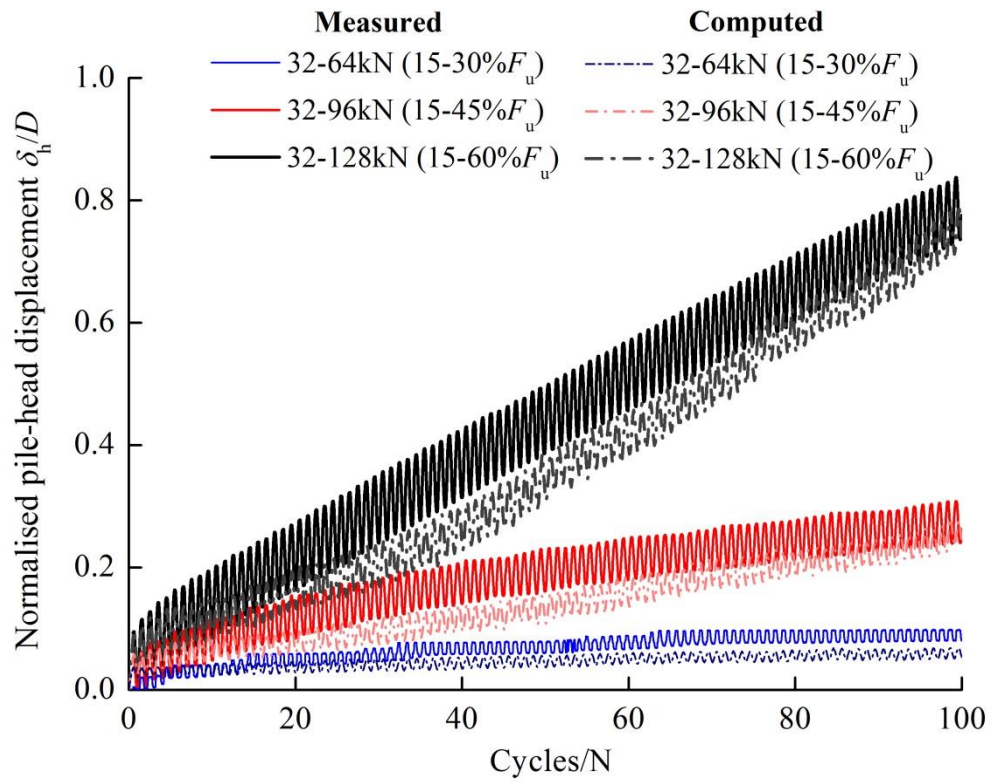


Fig. 16. Comparison of the measured and computed cumulative lateral pile head displacement

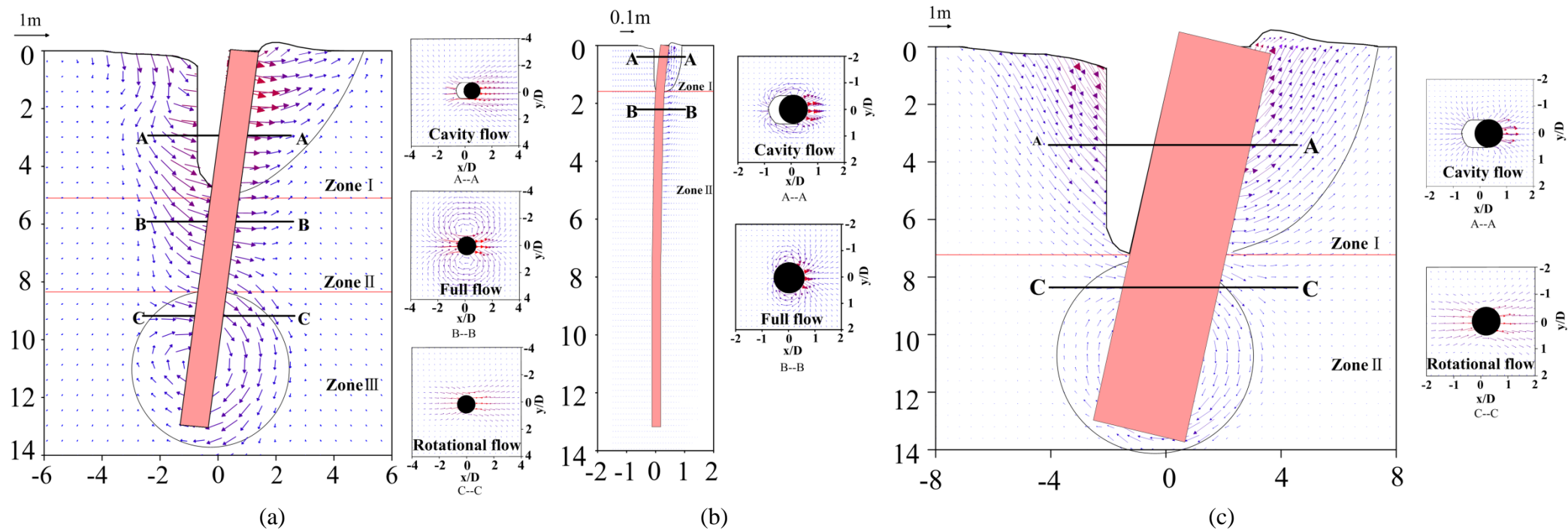
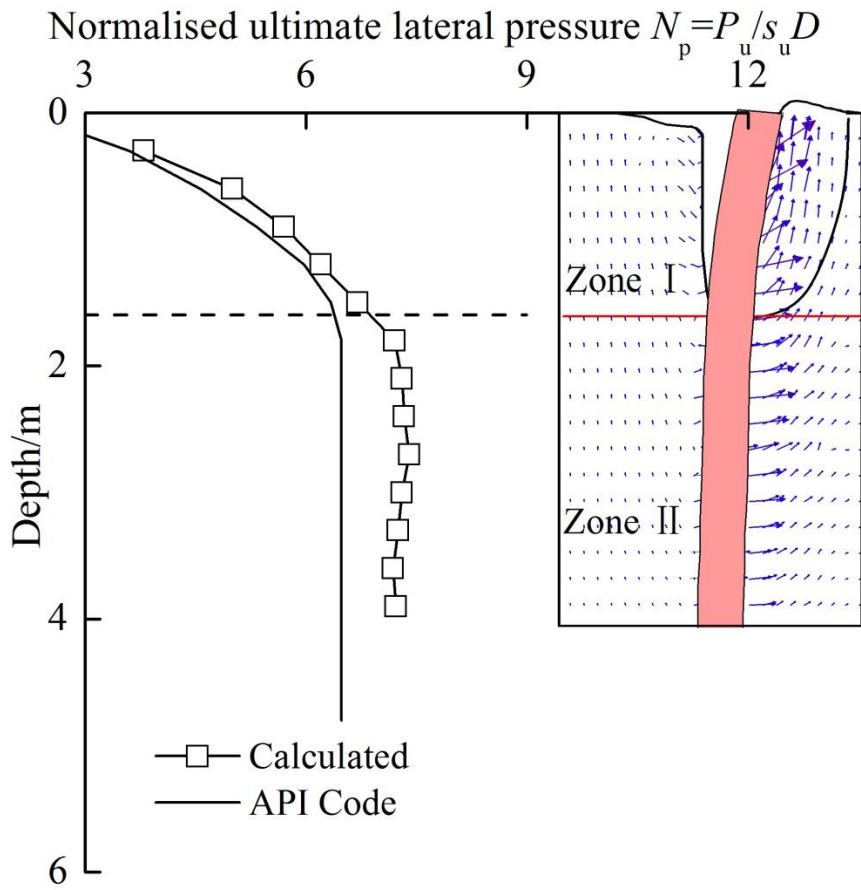
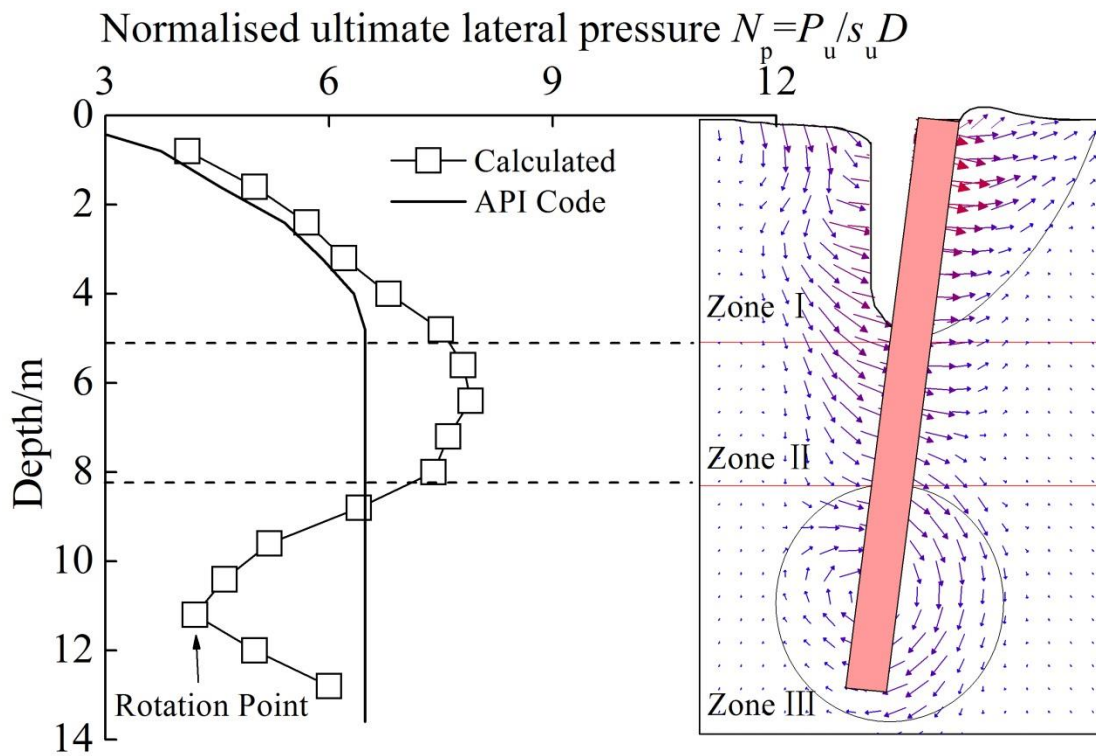


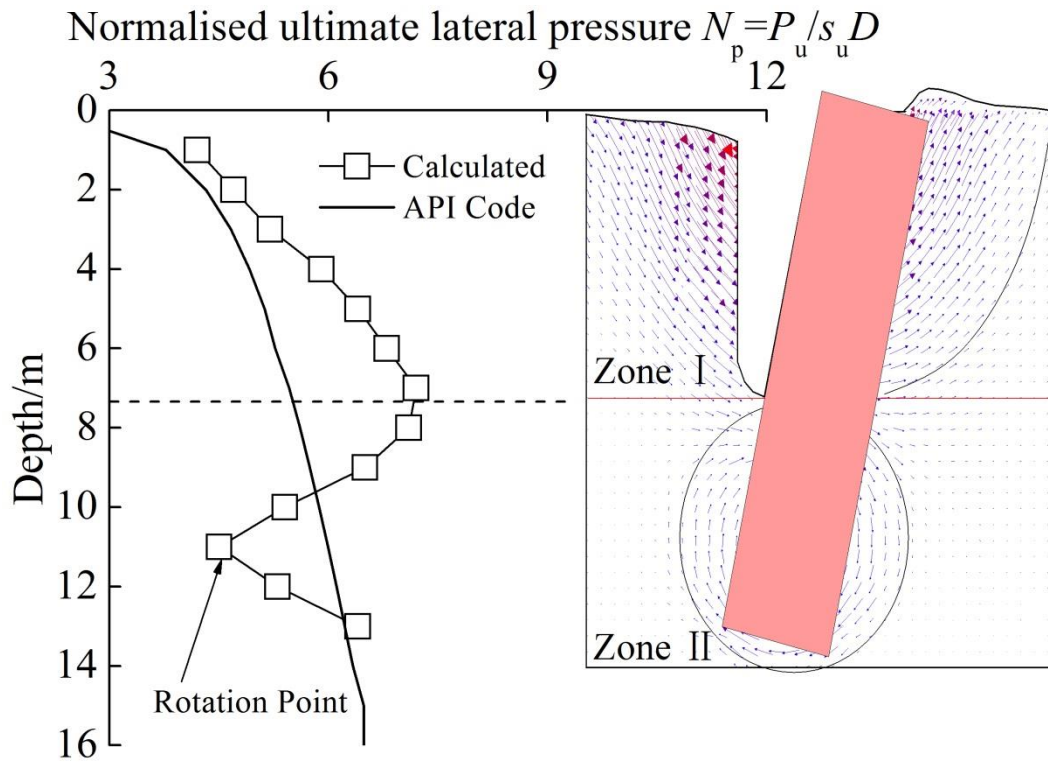
Fig. 17. Computed soil flow mechanisms around cyclically loaded piles with various diameters: (a) semi-rigid pile ($D=0.8\text{m}$); (b) flexible pile ($D=0.3\text{m}$); and (c) rigid pile ($D=4\text{m}$)



(a)



(b)



(c)

Fig. 18. Computed lateral bearing capacity factors along pile depth: (a) flexible pile ($D=0.3\text{m}$); (b) semi-rigid pile ($D=0.8\text{m}$); and (c) rigid pile ($D=4\text{m}$).

Caption of Tables

- | | |
|---------|--|
| Table 1 | Summary of relative pile-soil stiffness in previous studies on lateral loaded piles in soft clay |
| Table 2 | Centrifuge test programme and objective |
| Table 3 | Model parameters of kaolin clay |

Table 1 Summary of relative pile-soil stiffness in previous studies on lateral loaded piles in soft clay

| Reference | Bending stiffness of pile $E_p I_p$ (MNm ²) | Embedded depth of the pile l_L (m) | Average soil stiffness E_s (MPa) | Relative pile-soil stiffness $\frac{E_p I_p}{E_s l_L^4}$ | Pile rigidity |
|--------------------------------|---|--|---------------------------------------|---|---------------|
| Matlock (1970) | 114 | 12.8 | 8.00 | 0.00052 | flexible |
| Georgiadis (1992) | 0.00023 | 0.5 | 11.2 | 0.000326 | flexible |
| Mayne <i>et al.</i> (1995) | 3.31 | 1.1 | 11.2 | 0.244176 | rigid |
| Jeanjean (2009) | 913 | 20.2 | 6 | 0.000913 | flexible |
| Zhang <i>et al.</i> (2011) | 237 | 4.5 | 2.4 | 0.240 | rigid |
| Khemakhem <i>et al.</i> (2012) | 870 | 16.0 | 5.6 | 0.002438 | flexible |
| Wang <i>et al.</i> (2015) | 719 | 29.0 | 6 | 0.000169 | flexible |
| Haideraliet <i>al.</i> (2015) | 661436 | 20.0 | 7.8 | 0.52999 | rigid |
| Muraliet <i>al.</i> (2015) | 47819 | 7.1 | 3.2 | 5.88 | rigid |

Note: According to the criterion proposed by Poulos and Hull (1989), the upper bound and lower bound of

$\frac{E_p I_p}{E_s l_L^4}$ for flexible and rigid piles are 0.0025 and 0.208, respectively.

Table 2 Centrifuge test programme and objective

| Test ID | Pile type | Loading type | Objective |
|---------|---|--------------|--|
| 1 | Full model | Monotonic | Determining ultimate lateral pile capacity |
| 2 | Semi-rigid pile Full model | Cyclic | Understanding lateral cyclic response |
| 3 | Half model (for PIV analysis) | Cyclic | Revealing soil flow mechanism |
| 4 | Semi-rigid pile with jet-grouting Full model | Cyclic | Understanding lateral cyclic response |
| 5 | Half model (for PIV analysis) | Cyclic | Revealing soil flow mechanism |

1

Table 3 Model parameters of kaolin clay

| | Parameter | | Value | Remark |
|---|--|--|------------------|--|
| Monotonic response at medium to large strain levels | Critical state friction angle | ϕ' | 22° | Powrie (1986) |
| | Slope of the isotropic NCL in the $\ln(1+e) - \ln p'$ space | λ^* | 0.11 | Al-Tabbaa (1987) |
| | Slope of the isotropic unloading line in the $\ln(1+e) - \ln p'$ space | κ^* | 0.026 | |
| | Position of the isotropic NCL in the $\ln(1+e) - \ln p'$ space | N | 1.36 | |
| | | Parameter controlling the proportion of bulk and shear stiffness | ν | 0.1 |
| Cyclic response and small-strain stiffness upon various strain reversal | Strain range of soil elasticity | R | 1e ⁻⁴ | Calibrated against Benz's (2007) small-strain stiffness data |
| | Path-dependent parameter | m | 0.7 | |
| | Strain-dependent parameter 1 | β_r | 0.12 | |
| | Strain-dependent parameter 2 | χ | 5 | Calibrated against He's (2016) cyclic triaxial test results |
| | Stress-dependent parameter 1 | A_g | 650 | |
| | Stress-dependent parameter 2 | n_g | 0.65 | |

2

3